

Saturated-State Turbulence and Structure from Thermal and Magnetorotational Instability in the ISM: Three-Dimensional Numerical Simulations

Robert A. Piontek and Eve C. Ostriker

*Department of Astronomy
University of Maryland
College Park, MD 20742-2421*

rpiontek@astro.umd.edu, ostriker@astro.umd.edu

ABSTRACT

This paper reports on three-dimensional numerical simulations of dynamics and thermodynamics in the diffuse interstellar medium (ISM). Our models are local, account for sheared galactic rotation, magnetic fields, and realistic cooling, and resolve scales $\approx 1 - 200$ pc. This combination permits the study of quasi-steady-state turbulence in a cloudy medium representing the warm/cold atomic ISM. Turbulence is driven by the magnetorotational instability (MRI); our models are the first to study the saturated state of MRI under strongly inhomogeneous conditions, with cloud/intercloud density and temperature contrasts ~ 100 . For volume-averaged densities $\bar{n} = 0.25 - 4$ cm $^{-3}$, the mean saturated-state velocity dispersion ranges from $8 - 1$ km s $^{-1}$, with a scaling $\delta v \propto \bar{n}^{-0.77}$. The MRI is therefore likely quite important in driving turbulence in low-density regions of the ISM, both away from the midplane in the inner Galaxy (as observed at high latitudes), and throughout the far outer Galaxy (where the mean density drops and the disk flares). The MRI may even be key to suppressing star formation at large radii in spiral galaxies, where the pressure can be high enough that without MRI-driven turbulence, a gravitationally-unstable cold layer would form. As expected, we find that turbulence affects the thermal structure of the ISM. In all our simulations, the fraction of thermally-unstable gas increases as the MRI develops, and in the saturated state is largest in high- δv models. The mass fractions of warm-stable and unstable gas are typically comparable, in agreement with observations. While inclusion of resistive dissipation of magnetic fields could enhance the amount of thermally-unstable gas compared to current models, our present results indicate that even high levels of turbulence cannot wipe out the signature of thermal instability, and that a shift to a “phase continuum” description is probably unwarranted. Instead, we find that temperature

and density PDFs are broadened (and include extreme departures from equilibrium), but retain the bimodal character of the classical two-phase description. Our presentation also includes results on the distribution of clump masses (the mass spectrum peaks at $\sim 100 M_{\odot}$), comparisons of saturated-state MRI scalings with single-phase simulation results (we find $\langle B^2 \rangle$ is independent of \bar{n}), and examples of synthetic HI line profile maps (showing that physical clumps are not easily distinguished in velocity components, and vice versa).

Subject headings: galaxies: ISM — instabilities — ISM: kinematics and dynamics — ISM: magnetic fields — MHD

1. Introduction

Far from the energizing regions of star formation in the Milky Way and other galaxies, the interstellar medium (ISM) is still roiling with activity, and rife with structure. Both the microphysical properties and turbulent activity have been increasingly well characterized by Galactic and extragalactic radio observations. In particular, recent high-resolution Galactic emission surveys in the 21 cm hydrogen line (e.g. McClure-Griffiths et al. (2001); Taylor et al. (2003)), combined with Galactic absorption surveys (e.g. Heiles & Troland (2003); Mohan, Dwarakanath, & Srinivasan (2004)), and mapping of face-on external galaxies (e.g. Dickey et al. (1990); van Zee & Bryant (1999)), have begun to provide a wealth of thermal and kinematic information about the atomic ISM component, which comprises the majority of the total ISM mass in most spiral galaxies. Analysis of this data promises to yield a detailed empirical description of the atomic gas, which is known to consist of both warm and cold components, and to be strongly turbulent (e.g. Dickey & Lockman (1990)).

As observations of the ISM advance, there is a need on the theoretical side for increasingly sophisticated ISM modeling. With modern computational tools, it is possible to pursue time-dependent hydrodynamic models which incorporate many physical processes. This numerical modeling can extend established “classical” results for simplified systems into more realistic regimes, and test conceptual proposals for the behavior of complex systems in a rigorous fashion. The goal of detailed ISM modeling, of course, is not sophistication for its own sake, but to gain understanding about how different “elemental” processes interact, to ascertain which among many contributing processes are most important, and to aid in interpreting and developing reliable physical diagnostics from observations.

Broadly, the presence of structure in the atomic ISM can be easily understood as a consequence of the bistable thermal equilibrium curve over a range of pressures, including

those typical of the ISM. Since the temperatures of the two stable thermal equilibria differ by a factor of ~ 100 (at fixed pressure), the “classical” expectation based on the principle of pressure equilibrium is a system of cold, dense clouds embedded in a much more diffuse warm intercloud medium (Field, Goldsmith, & Habing 1969). Thermal instability (TI) tends to move gas parcels at intermediate temperatures into one of the stable phases (Field 1965). Clouds are initially expected to condense at preferred scales where conduction limits local thermal gradients. While these basic processes are certainly involved in establishing the ISM’s structure, the end result is a complex product of evolution and interactions with other physical processes, leaving many open questions. For example, how do the agglomerations and disruptions of cold clouds depend on the turbulence properties, and how does this affect the mass function of condensations that results?

Many processes have been proposed that can produce turbulence in the ISM (see e.g. Mac Low et al. (2004); Elmegreen & Scalo (2004) for recent reviews). Traditionally, turbulence is thought to be driven primarily by supernovae (McKee & Ostriker 1977) (and, to a lesser extent, expanding HII regions), because the total kinetic energy they are able to supply could be sufficient to offset the turbulent dissipation in the Milky Way’s diffuse ISM (Spitzer 1978, Ch. 11). Supernovae are certainly the primary source of turbulence near regions of high-mass star formation. However, it is not clear how effectively this energy can in fact be shared with the bulk of the ISM, so other sources may be (or combine to be) of comparable importance. Indeed, observations indicate that the levels of turbulence are not strongly correlated with spiral arms (where star formation is enhanced), and are just as large in outer galaxies (where overall star formation rates are low) as in inner regions (van Zee & Bryant 1999; Petric & Rupen 2001). Moreover, recent 3D simulations (Korpi et al. 1999; de Avillez & Breitschwerdt 2005) in which turbulence is driven solely by supernovae find that velocity dispersions are significantly lower in cold gas than in warm gas, inconsistent with observations (Heiles & Troland 2003).

An obvious non-stellar energy source for the ISM is galactic rotation. Wherever the angular velocity decreases outward and magnetic fields are present, the powerful magnetorotational instability (MRI) is expected to tap this rotation and drive large-amplitude ISM turbulence (Sellwood & Balbus 1999; Kim, Ostriker, & Stone 2003; Dziourkevitch, Elstner, & Rüdiger 2004). Detailed development of MRI has primarily been studied in adiabatic or isothermal gas, where turbulent velocities and Alfvén speeds grow into rough equipartition at slightly subsonic levels (e.g. Hawley, Gammie, & Balbus (1995, 1996) hereafter HGB1, HGB2)). Adiabatic and isothermal models, however, are essentially single phase, with only small variations in density and temperature. How do turbulent saturation levels differ in a medium where there are huge variations in conditions, such that subsonic speeds with respect to the diffuse gas are highly supersonic with respect to the dense gas?

In the real ISM, dynamics must affect thermodynamics, and vice versa. The turbulent power input is significant, and both (irreversible) dissipative heating and (reversible) PdV heating and cooling can alter distributions of temperatures compared to the narrow spikes at warm and cold equilibria that would otherwise occur. In turn, thermodynamics potentially can affect loss rates of turbulence: supersonic compressions are dissipative while subsonic compressions are not, and dissipation of magnetic energy by reconnection depends on local conditions of density and temperature. Cloudy structure also changes effective flow “collision” times, as well as field line geometry. Indeed, recent observational evidence has shown that the fraction of unstable gas in the ISM may be significant; Heiles & Troland (2003) found that at high latitudes, about half the warm neutral medium (WNM) lies at thermally unstable temperatures between 500-5000 K. Numerical models which include effects of star formation (Rosen & Bregman 1995; Korpi et al. 1999; de Avillez 2000; Wada, Spaans, & Kim 2000; Gazol et al. 2001; Wada & Norman 2001; Wada 2001; Mac Low et al. 2004; Slyz et al. 2004) find both turbulence and significant fractions of unstable gas, although it is not clear how much the temperature distributions are affected by the direct heat inputs in the star formation feedback algorithms of these models.

Recent simulations have addressed nonlinear evolution, in 2D and 3D, of TI in the ISM without “stellar” energy inputs (Hennebelle & Pérault 1999; Burkert & Lin 2000; Vázquez-Semadeni, Gazol, & Scalo 2000; Sánchez-Salcedo, Vázquez-Semadeni, & Gazol 2002; Kritsuk & Norman 2002; Vázquez-Semadeni et al. 2003; Audit & Hennebelle 2004; Kritsuk & Norman 2004), and there have also been many numerical studies, in 2D and 3D, of the MRI in single-phase gas. In previous work, we performed 2D studies of TI and MRI in combination (Piontek & Ostriker (2004), hereafter Paper I). Paper I showed that MRI growth rates in a two-phase medium are comparable to those in a single-phase medium with the same $\bar{\rho}$ and $\bar{\mathbf{B}}$, provided that the cloud separation along field lines does not exceed half of the fastest-growing MRI wavelength (typically ~ 100 pc). Although there have been suggestions that TI itself could be a significant source of turbulence, “pure TI” models we performed show that for pressures comparable to mean galactic values (i.e. away from HII regions or recent supernovae), velocity dispersions are only a few tenths of a km s^{-1} . In our 2D simulations, the MRI leads to large-amplitude velocities and magnetic fields, but as for single-phase 2D models, late time behavior is dominated by the “channel flow;” quasi-steady turbulence is possible only for 3D flows. The present work constitutes the extension of Paper I to 3D, in order to study the saturated state of MRI in the presence of a two-phase medium. As we shall describe, we have performed a variety of simulations, with parameters covering a range of conditions characteristic of the atomic ISM.

The plan of this paper is as follows: In §2 we briefly describe the numerical method, and the initializations for the various models we have performed. In §3 we present the results

of our simulations in terms of the models’ physical structure, thermodynamic distributions, and turbulent states (in velocities and magnetic fields), as well as exhibiting sample synthetic observations based on our simulated data. We summarize, discuss the astronomical implications of our results, and compare to previous work in §4.

2. Numerical Methods and Model Parameters

The numerical methods utilized for the present study are essentially the same as those of Paper I, but extended from 2D to 3D. For a complete description of the numerical method and tests, please see that work. Here, we briefly summarize the salient points.

We integrate the time-dependent equations of magnetohydrodynamics with a version of the ZEUS code (Stone & Norman 1992a,b). ZEUS uses a time-explicit, operator-split, finite difference method for solving the MHD equations on a staggered mesh, capturing shocks via an artificial viscosity. Velocities and magnetic field vectors are face-centered, while energy and mass density are volume-centered. ZEUS employs the CT and MOC algorithms (Evans & Hawley 1988; Hawley & Stone 1995) to maintain $\nabla \cdot \mathbf{B} = 0$ and ensure accurate propagation of Alfvén waves.

We have implemented volumetric heating and cooling terms, and a thermal conduction term. The update due to net cooling is solved implicitly using Newton-Raphson iteration. For a given hydrodynamical time step, the change in temperature in each zone is limited to be less than 25%. This is a somewhat larger fraction than the 10% limit used in Paper I, which allows us to run with larger time steps needed to make 3D calculations practical. Tests have shown that relaxing this constraint does not affect cloud structure; ΔT exceeds 10% only in a very small fraction of zones. The conduction term is solved explicitly using a seven point stencil for the second derivative of temperature. We also model the differential rotation of the background flow and the variation of the stellar/dark matter gravitational potential in the local limit with $x \equiv R - R_0 \ll R_0$, where R_0 is the galactocentric radius of the center of our computational domain. The equations we solve are therefore:

$$\frac{\partial \rho}{\partial t} + \nabla \cdot (\rho \mathbf{v}) = 0 \quad (1)$$

$$\frac{\partial \mathbf{v}}{\partial t} + \mathbf{v} \cdot \nabla \mathbf{v} = -\frac{\nabla P}{\rho} + \frac{1}{4\pi\rho}(\nabla \times \mathbf{B}) \times \mathbf{B} + 2q\Omega^2 x \hat{x} - 2\Omega \times \mathbf{v} \quad (2)$$

$$\frac{\partial \mathcal{E}}{\partial t} + \mathbf{v} \cdot \nabla \mathcal{E} = -(\mathcal{E} + P)\nabla \cdot \mathbf{v} - \rho \mathcal{L} + \nabla \cdot (\mathcal{K} \nabla T) \quad (3)$$

$$\frac{\partial \mathbf{B}}{\partial t} = \nabla \times (\mathbf{v} \times \mathbf{B}) \quad (4)$$

All symbols have their usual meanings. The net cooling per unit mass is given by $\mathcal{L} = \rho\Lambda(\rho, T) - \Gamma$. We adopt the simple atomic ISM heating and cooling prescriptions of Sánchez-Salcedo, Vázquez-Semadeni, & Gazol (2002), in which the cooling function, $\Lambda(\rho, T)$, is a piecewise power-law fit to the detailed models of Wolfire et al. (1995). The heating rate, Γ , is taken to be constant at $0.015 \text{ erg s}^{-1}\text{g}^{-1}$. In the tidal potential term of equation (2), $q \equiv -d \ln \Omega / d \ln R$ is the local dimensionless shear parameter. We adopt q equal to unity, to model a flat rotation curve in which the angular velocity $\Omega \propto R^{-1}$.

The present set of simulations is 3D, with the computational domain representing a cubic sector of the ISM in the radial-azimuthal-vertical ($x - y - z$) domain. We employ shearing-periodic boundary conditions in the \hat{x} -direction (Hawley & Balbus 1992; Hawley, Gammie, & Balbus 1995), and periodic boundary conditions in the \hat{y} - and \hat{z} -directions, as originally implemented in ZEUS by Stone et al. (1996). This framework allows us to incorporate realistic galactic shear, while avoiding numerical artifacts associated with simpler boundary conditions. We have previously used an isothermal version of the same code to study larger-scale galactic ISM problems (Kim, Ostriker, & Stone 2002, 2003).

We have parallelized the code with MPI to run on distributed-memory platforms. We perform a standard domain decomposition in \hat{x} , so that each processor works on a slab of the domain. Decomposing in \hat{y} and \hat{z} as well would reduce message-passing time when running on more than eight processors, but for gigabit networks and faster the compute time exceeds the message-passing time for 128 or fewer processors in any case. Thus, for our moderate problem sizes, the additional effort that would be required to parallelize the shearing-periodic boundary conditions is not merited.

Our standard resolution is 128^3 zones. To confirm numerical convergence, we also performed one simulation at 256^3 and found the results to be similar to the standard resolution run. Our box is 200pc on each side, giving a resolution of about 0.8 pc in our 256^3 run, and about 1.6 pc in our 128^3 resolution runs. We set the conduction coefficient to $\mathcal{K} = 1.03 \times 10^7 \text{ ergs cm}^{-1} \text{ K}^{-1} \text{ s}^{-1}$. This level of conduction was chosen to allow us to resolve all modes of TI that are present (see Paper I). In our fiducial model, the initial state of the gas is constant density, constant pressure with conditions comparable to mean values in the solar neighborhood; $n = 1.0 \text{ cm}^{-3}$ and $P_0/k = 2000 \text{ K cm}^{-3}$. The corresponding initial isothermal sound speed is $c_s = 3.6 \text{ km s}^{-1}$. The initial magnetic field strength satisfies $\beta = P_{\text{gas}}/P_{\text{mag}} = 100$, corresponding to $B = 0.26 \mu\text{G}$ in the vertical (\hat{z}) direction. This is our “standard” run. Additional simulations are performed with varying mean den-

sities of $n = 0.25, 0.67, 1.5$ and 4.0 cm^{-3} , as well as one with lower magnetic field strength, $\beta = P_{\text{gas}}/P_{\text{mag}} = 1000$. We also performed an isothermal simulation with $c_s = 2.8 \text{ km s}^{-1}$ and $n = 1.0 \text{ cm}^{-3}$. This value of c_s was chosen so that the initial thermal pressure matches the mean late-time pressure in our cooling models. Finally, we also performed a simulation with heating and cooling turned on that was initialized from the saturated-state, turbulent isothermal model. For all our models we adopt the galactic orbital period at the solar radius, $2.5 \times 10^8 \text{ yr}$, to normalize the shear rate.

Since increasing or decreasing the mean density by a large factor relative to $n = 1 \text{ cm}^{-3}$ would initialize the gas in a thermally *stable* state, some of our simulations are initialized with a medium already in a two-phase state, rather than with a uniform density. For these models, spherical clouds of cold dense gas are inserted into a warm ambient medium at random locations. The number of clouds is adjusted so that the average density of the cloudy medium is at the desired level. A similar simulation was performed in Paper I, which allowed us to study the growth rates of the MRI in an initially quiescent cloudy medium. Since the 2D simulations of Paper I were axisymmetric there was no evolution of the model until MRI modes began to grow. This allowed us to compare directly the MRI growth rates of an adiabatic run with a two-phase run, illustrating the effect of cloud size and distribution on the growth rates. In the present 3D simulations, however, the evolution is rapid because the symmetry in the azimuthal direction is broken. Individual clouds are sheared out relatively quickly, and also begin to merge with nearby clouds. Nevertheless, because MRI-driven turbulence eventually dominates both the initially-thermally-unstable and initially-two-phase models, at late times the two are indistinguishable.

On top of the initial conditions given above, we add pressure perturbations with a white noise spectrum at the 0.1% level to seed the TI and MRI. In the next section, we describe results from our standard run in detail, and comment on differences with the other runs as is appropriate.

3. Results

3.1. Overall Evolution

Figures 1 and 2 are volume renderings of the 3D density data cube, from our run with fiducial parameters, and resolution 256^3 , at $t = 1.0$ and 9.0 orbits. The early development of both TI and MRI in the present set of 3D simulations is quite similar to the development previously described for 2D simulations in Paper I. Initially the gas is thermally unstable. The cooling time scale is much shorter than the orbital time scale, and the gas quickly

separates into many small, cold clouds embedded in a warm ambient medium. This phase of the evolution lasts about 20 Myr, which is comparable to the 2D simulations of Paper I. The typical size scale of the clouds is about 5 pc, consistent with expectations for the fastest growing modes at the adopted level of conductivity. The size scale of the clouds is still fairly close to its initial distribution in Figure 1 at $t = 1.0$ orbits.

After the initial condensation phase of TI is complete, large scale galactic shear begins to drive the evolution. Already at $t = 2.0$ orbits, the clouds have become elongated in the \hat{y} direction. During the first few orbits interactions take place between nearby clouds, which typically lead to mergers, increasing the typical size scale significantly. At about $t = 4.0$ orbits ($= 10^9$ yrs) the modes of the MRI have grown significantly and now begin to dominate the evolution of the model. The simulation becomes fully turbulent, drastically altering the dynamics compared to the axisymmetric model of Paper I. Shear from the MRI with velocities in all directions, combined with galactic shear with velocities in the azimuthal direction, leads to repeated disruptive interactions and collisions between clouds. Clouds merge into an interconnected network, with individual entities existing for only short periods of time. It is difficult to convey the dynamical nature of the simulations to the reader using only snapshots in time; the animation associated with Figures 1-2 shows this much more clearly.

While the structure remains highly dynamic, a quasi-equilibrium saturated state is established by $t \sim 5$ orbits, and the statistical properties of the gas remain relatively constant throughout the latter half of the simulation (up to $t=10$ orbits). The approach to a quasi-steady turbulent state in these models is generally similar to the results for isothermal or adiabatic single phase models (e.g. HGB1, HGB2). In the remainder of §3, we discuss details of evolution and quasi-steady properties, similarities and differences from single-phase models, and dependencies on model parameters.

3.2. Density Structure

The density probability distribution functions (PDFs) from our standard run (at 128^3) are shown in Figure 3 at $t = 1, 2.5, 5.0$, and 9 orbits. We show both mass-weighted and volume-weighted density PDFs in Panels A-D, and compare the PDFs of the 128^3 and 256^3 runs in Panel D. Similar to our results in Paper I, we find that by mass, most of the gas is in the cold phase, while the warm phase occupies most of the volume. After the initial development of TI has completed, at $t = 1.0$ orbits, the mass fraction of gas in the warm (F), unstable (G), and cold (H) phases is 14%, 5%, and 80%, respectively. By volume, 83%, 9%, and 8% of the gas resides in the warm, unstable, and cold phases. From $t = 1.0$ to

$t = 2.5$ orbits (panels A and B of Figure 3) the evolution is driven mainly by galactic shear. The size distribution of the clouds shifts to larger masses through mergers, but the density PDFs over this interval vary little. The fraction of gas in each phase changes by only a few percent during this time period.

In contrast, between $t = 2.5$ and $t = 5.0$, Panels B and C of Figure 3, the evolution changes from being driven primarily by galactic shear, to being driven primarily by the MRI. The model becomes fully turbulent, and this has a significant effect on the detailed shape of the density PDF. The fractions of gas in the warm, unstable, and cold phases at $t = 5.0$ are now 10%, 7%, and 83% by mass, and 84%, 8%, and 7% by volume. Near the end of the simulation, at $t = 9$, the gas fractions are 14%, 18%, and 67% percent by mass and 82%, 10%, and 6% percent by volume. From $t = 5$ to $t = 9$, (Panel D of Figure 3) the PDF remains very similar, indicating that the model has reached a quasi-steady state. At late times, gas is found at both lower and higher densities than was previously observed before the development of the MRI. Thus, the magnetized turbulence induces both strong compressions and significant rarefactions. Compared to the maximum (ρ_{\max}) and minimum (ρ_{\min}) densities before the onset of turbulence, ρ_{\max} increases by an order of magnitude and ρ_{\min} decreases by a factor of about 3. The fraction of gas in the intermediate density regime is a factor 2 – 3 larger after the full development of MRI compared to early on. The proportion of thermally-unstable gas is never greater than 20% of the whole (for this set of parameters), but exceeds the proportion of thermally-stable warm gas during the turbulent stages of evolution.

To investigate properties of individual condensations in our model, we use an algorithm similar to that of CLUMPFIND (Williams et al. 1994). The algorithm was developed and applied by Gammie et al. (2003) to identify clumps in simulations of turbulent molecular clouds. Briefly, the algorithm first finds all local maximum values of density in the computational volume. All grid cells with a density higher than a chosen threshold density, n_t , are assigned to the nearest local maximum. This set of continuous zones defines a clump. The only other parameter needed is a smoothing length, applied to the initial density data cube (see Gammie et al. 2003); we set this to 1.5 grid zones. In Figure 4 we show the clump mass spectrum for two different choices of threshold density, $n_t = 8$ and 20 cm^{-3} . This mass spectrum is computed at $t = 6.5$ orbits. Mass spectra from other late times are similar. With $n_t = 8 \text{ cm}^{-3}$, 812 clumps were found, with a minimum clump mass of $5.6 M_{\odot}$, and a maximum mass of $2800 M_{\odot}$. For reference, the total mass in the simulation is $2.51 \times 10^5 M_{\odot}$. Increasing the critical density to $n_t = 20 \text{ cm}^{-3}$, we find 168 clumps, with a minimum mass of $35 M_{\odot}$, and a maximum mass of $2200 M_{\odot}$. For both cases, the peak of the mass spectrum is in the range $100 - 300 M_{\odot}$; the peak increases slightly for larger n_t .

To describe their shapes, we compute diagonalized moment of inertia tensors for each clump, following Gammie et al. (2003). Figure 5 plots the ratios, for each clump, of the smallest (c) and intermediate (b) axes to the largest (a) axis. Prolate-shaped clumps lie near the diagonal line, oblate clumps lie near the right side vertical axis, and triaxial clumps lie in the center. Using two dotted lines to demarcate these groups, we find 38 % of the clumps are prolate, 49 % are triaxial, and 14% are oblate. Although clumps are certainly not round, typical minimum to maximum axis ratios are about 2:1. “Filaments”, with $c/a=0.1$ are common, however, and these elongated structures are easy to pick out in Figure 2.

3.3. Pressure and Temperature Structure

The pressure PDFs at $t = 1, 2.5, 5$, and 9 orbits are presented in Figure 6. At $t = 1$, most of the gas falls within a narrow range of pressures, $P/k=900-1300 \text{ K cm}^{-3}$. This is lower than $P/k=2000 \text{ K cm}^{-3}$ in the initial conditions, due to systematic cooling in the thermally unstable stage of evolution. The pressure PDF changes little from $t = 1$ to $t = 2.5$ orbits, shown in panels A and B of Figure 6. With the development of MRI, however, gas is driven to both higher and lower pressures, as can be seen in Panels C and D, at $t = 5$ to $t = 9$ orbits. The mean volume-weighted pressure at the end of the simulation is slightly lower than that after TI has developed, about $P/k=1200 \text{ K cm}^{-3}$. The pressures in the cold and warm phases are approximately equal in the latter half of the simulation, while the pressure in the intermediate phase is slightly higher, about $P/k=1300 \text{ K cm}^{-3}$. The dispersion in pressure early in the simulation is about $\delta P/k \sim 60 \text{ K cm}^{-3}$, while late in the simulation this increases to as much as $\delta P/k \sim 400 \text{ K cm}^{-3}$.

In Figure 7 we show scatter plots of pressure against density overlayed on our model cooling curve at $t = 1, 2.5, 5$, and 9 orbits. We also show contours of constant temperature to indicate the transitions between different phases of gas. Only a fraction of the zones are included because of the large number of cells contained in our 3D simulations. Early in the simulation (Panels A and B), the gas is close to pressure equilibrium, although high density gas lies closer to the thermal equilibrium curve. Later in the simulation (Panels C and D), strong interactions between clouds can drive gas far from pressure equilibrium. At low densities where the cooling time scale is longer than the dynamical time, gas can be found at pressures as high as $P/k=3200 \text{ K cm}^{-3}$ and as low as 800 K cm^{-3} , a range of a factor four. Much of the low-density gas is not in thermal equilibrium. In high density regions there is also a wide range of pressures observed ($P/k=800-4000 \text{ K cm}^{-3}$), but because the cooling time is very short ($\sim 10^4 \text{ yr}$) this gas maintains thermal equilibrium. At early times, distributions of density and pressure are quite similar to the corresponding results from our

2D models (Paper I) after the nonlinear development of TI. At late times, however, these 3D turbulent models show much broader pressure distributions than our 2D models. Overall, the mean pressure averaged over orbits 6-10 is 1206 K cm^{-3} . By phase the mean pressure is $P/k = 1187, 1324$, and 1195 K cm^{-3} in the warm, intermediate and cold phases.

Also of interest are the temperature PDFs, shown in Figure 8 at the same times as in Figure 3. In Panels C and D, the fraction of gas in the intermediate temperature phase has increased, and gas is also found at colder temperatures than are present earlier in the simulation. The minimum temperature is 80K, and respectively 60% and 68% of the gas mass is found between 80-120K at $t = 1$ and 2.5 orbits. At $t = 5$ and 9 orbits, on the other hand, respectively 30% and 18% of the gas is found at temperatures below 80K, while respectively another 32% and 31% of gas is at $T=80-120 \text{ K}$. The range of temperatures in which the majority of cold gas is found increases by about a factor of two. The upper limit on temperature increases slightly throughout the run, but in addition, the dispersion of temperatures in the warm medium increases. At early times, $\sim 80\%$ of the warm gas is in the range $T=6600-8600 \text{ K}$, whereas at late times, 80% is evenly distributed over twice as large a spread in temperatures.

Figure 9 compares the volume-weighted temperature PDFs of four runs of different mean density. These four runs have average densities of $\bar{n} = 4.0, 1.5, 1.0$, and 0.67 cm^{-3} and, as we shall discuss in §3.4, the mean velocity dispersion increases by an order of magnitude from the highest to lowest mean density models. The PDFs in Figure 9 represent averages from 6.0-6.5 orbits. At intermediate and high temperatures, the PDFs for these runs are quite similar. Most of the warm gas is at $T=6000-8000 \text{ K}$, with $T_{\max} \approx 10000 \text{ K}$. Most of the cold phase is at temperatures near 100 K, possibly showing a slight trend towards higher mean temperature as \bar{n} is decreased. Overall there is less gas at lower temperature when \bar{n} is reduced, because the total mass available for cold clouds is lower. In addition to having similar warm and cold gas temperatures, the models with various \bar{n} are similar in that the fractions of gas in the intermediate- and warm-temperature regimes are always quite close. These results are illustrated in Figure 10, which plots the mass fractions in the various regimes as a function of \bar{n} (also including the $\bar{n} = 0.25$ model).

Overplotted in Figure 10 are curves indicating the warm and cold gas mass fractions that a pure two-phase medium would have. The mass fraction of cold gas in a perfect two-phase medium in thermal and pressure equilibrium is $f_c = (1 - n_w/\bar{n})/(1 - n_w/n_c) \approx 1 - n_w/\bar{n}$, where n_c is the cold density, n_w is the warm density, and \bar{n} is the mean density. The mass fraction of warm gas is then $f_w \approx n_w/\bar{n}$. The density of warm gas in our simulations is typically $n_w = 0.25$, which we use to compute the theoretical curves in Figure 10.

The possibility exists that our choice of initial conditions in the standard run, a uniform

medium at the average density, may have some effect on the amount of gas in the intermediate phase at late times. Due to TI, initially most of the gas collects into small, dense cold clouds, and only a small proportion of the gas remains in the thermally unstable regime. Later in the simulation, the MRI drives a larger fraction of gas into the unstable phase. It is possible that if we had *begun* with a turbulent medium, this fraction would be even larger, from increased shock heating of moderate density clouds with larger collision cross sections. To investigate this, we initialized a simulation with the same mean density and magnetic field as our standard run, but evolved it with an isothermal equation of state. The sound speed was set so that the initial P/k matches late time averages from our standard run. After the isothermal evolution has proceeded for 10 orbits and reached a saturated turbulent state, heating and cooling are enabled. After a quasi-steady state is reestablished, we measure the mass fractions in the warm, intermediate, and cold regimes. The result is respective proportions of about 11%, 14%, and 75%, which is similar to our results from standard run. Thus, we conclude that the long-term thermal history does not strongly affect the present state of the gas.

3.4. Turbulent Velocities

In Figure 11 we plot the mass-weighted Mach number $\mathcal{M} \equiv \delta v/c_s$ of the gas in each thermal phase (warm, intermediate, cold) as a function of time for the duration of the simulation. We also include, for comparison, the mass-weighted Mach number of the cold medium for the high resolution run at 256^3 . The isothermal sound speed $c_s = (kT/\mu)^{1/2}$ is computed individually for all grid zones, and the galactic shear is subtracted from the azimuthal (v_y) velocity before computing $\delta v^2 = v_x^2 + (\delta v_y)^2 + v_z^2$. Initially, motions in all three phases of the gas are subsonic, $\mathcal{M} < 0.3$, and remain so until the MRI begins to develop at about 800 Myr (~ 3 orbits). Once the MRI saturates (at $t \sim 5$ orbits), the typical Mach numbers of the warm, intermediate and cold phases of the gas are 0.4, 1.8, and 2.9. The peak value of \mathcal{M} for the cold phase is about 3.2. The mean late time velocity dispersion for all three phases of the gas is similar, approximately 2.7 km s^{-1} . At late times, the individual velocity dispersions in the radial, azimuthal, and vertical directions are 1.9, 1.7, and 0.7 km s^{-1} , respectively.

To explore the dependence of saturated state turbulence on system parameters, for our five simulations of varying mean density \bar{n} we have computed the average Mach number over $t = 5 - 10$ orbits. We plot the results, separating the three thermal phases, as a function of \bar{n} in Figure 12. The relationships between \mathcal{M} and \bar{n} clearly follow power laws. The slopes for the warm, intermediate and cold phases are $d \ln \mathcal{M} / d \ln \bar{n} = -0.67, -0.68$ and

-0.77. Since the cold component dominates the mass, this implies $(\delta v) \propto (\bar{n})^{-0.77}$ overall. For our $\beta = 1000$ model at $\bar{n} = 1 \text{ cm}^{-3}$, the saturated state Mach numbers are 0.3, 1.1, and 1.6 for the warm, intermediate, and cold phases. Our results are thus consistent with general findings from previous MRI simulations that saturated-state turbulent amplitudes increase with increasing mean Alfvén speed. The detailed scalings, however, show interesting differences, which we shall discuss in §4.

We have found that the turbulence is quite insensitive to particularities of structure in initial conditions. Thus, our model which began with a two phase “cloudy” medium, with the same initial mean density as our standard run, saturates with nearly the same velocity amplitude as the standard run. The initially-isothermal run which was restarted with cooling also yielded similar results to the standard run, with Mach numbers of 0.4, 1.7, and 2.8 for the warm, intermediate and cold phases. The saturated state of the isothermal simulation itself has a Mach number of 1.4, corresponding to mean velocity dispersion 4.0 km s^{-1} , somewhat larger than for our cooling models at this fiducial mean density. Differences between isothermal and multiphase models are likely to depend on \bar{n} , however.

The average Reynolds stress, $\langle \rho v_x \delta v_y \rangle / P_0$, from $t = 5 - 10$ orbits is plotted against the mean density for $\bar{n} = 4.0, 1.5, 1.0, 0.67$, and 0.25 cm^{-3} in Figure 13. The relationship again follows a power law, with a slope of -1.1.

The velocity power spectra are generally consistent with previous simulations of the MRI (Hawley, Gammie, & Balbus 1995; Kim, Ostriker, & Stone 2003). The largest scales dominate the simulation, generally following a Kolmogorov-like spectrum, $\sim k^{-11/3}$. Our quoted values for the velocity dispersions therefore correspond to the largest scales in the simulations. On smaller scales, such as an individual cloud, the velocity dispersion would be smaller. We have tested the relation between linewidth and size directly, using the “ROC” analysis approach described in Ostriker, Stone, & Gammie (2001). Both for the cold component alone, and for the whole medium, we find that the velocity dispersion increases with the size of clouds, or sub-boxes of the computational volume.

3.5. Magnetic Fields

Similarly to the (random) kinetic energy, the magnetic energy increases as the MRI develops. In Figure 14 we plot the magnetic field strength as a function of time for each of the three phases of gas. In the initial conditions, $B = B_z = 0.26 \mu\text{G}$. After TI develops, the field strength is $0.25 \mu\text{G}$ for the warm phase, and about $0.5 \mu\text{G}$ for the (denser) unstable and cold phases. As the MRI develops, after $t = 5$ orbits, the field strength grows to range

over $2 - 3 \mu\text{G}$ for all three phases, reaching as high as $4.1 \mu\text{G}$ in the cold phase. The late time component magnetic field strengths, $\langle B_x^2 \rangle^{1/2}$, $\langle B_y^2 \rangle^{1/2}$, and $\langle B_z^2 \rangle^{1/2}$ are 1.3, 1.9, and $0.51 \mu\text{G}$, averaged over $t = 6 - 10$ orbits. Thus, the MRI enhances the magnetic field by an order of magnitude over its initial value. We note that if overdense clouds were to form by isotropic contraction of the ambient medium, then one would expect $\langle B^2 \rangle^{1/2} \propto \rho^{2/3}$. With a cold medium density two orders of magnitude larger than that of the warm medium, the respective mean field strengths would differ by a factor 20. Since this is not the case, condensation evidently proceeds preferentially along field lines.

To explore dependence on mean properties, in Figure 15 the late time magnetic field strength, averaged over five orbits, is plotted against the mean density in the box for five simulations with $\bar{n} = 4.0, 1.5, 1.0$, and 0.67 cm^{-3} . Unlike the turbulent velocity dispersions, the B field strength does not show any significant trend with \bar{n} , saturating between 2 and $3 \mu\text{G}$. The field strength also does not differ significantly between the cold, intermediate, and warm phases for any of the models. As a marginal effect, the field strength in the warm medium decreases as \bar{n} increases.

Unlike the magnetic energy density, the Maxwell stress does show dependence on \bar{n} . This stress, $\langle -B_x B_y / 4\pi \rangle / P_0$, is averaged over $t = 5 - 10$ orbits and plotted against the mean density for five simulations with $\bar{n} = 4.0, 1.5, 1.0, 0.67$ and 0.25 cm^{-3} in Figure 16. For the data shown, a power law fit yields slope -0.42. Previous single-phase MRI simulations show somewhat different scalings of Maxwell stresses and magnetic energies, as we shall discuss in §4.

The power spectra of the magnetic field, like the velocity power spectra, is consistent with previous simulations of the MRI (Hawley, Gammie, & Balbus 1995; Kim, Ostriker, & Stone 2003), dominated by the largest scales and generally following a Kolmogorov-like spectrum.

3.6. Energetics

Tracking the changes in various energies is key to understanding the interrelationships between dynamics and thermodynamics in turbulent flows. For the models we have performed, the ultimate energy source is the shear flow, which drives the MRI. In turn, turbulent dissipation can convert kinetic and magnetic energy to thermal energy, which can subsequently be lost to radiation. More formally, following HGB1, we consider the average

over the box of the total energy per unit volume,

$$\langle \mathcal{H} \rangle = \left\langle \rho \left(\frac{1}{2} v^2 + \frac{\mathcal{E}}{\rho} - \frac{q\Omega^2 x^2}{2} \right) + \frac{B^2}{8\pi} \right\rangle. \quad (5)$$

Changes to this energy can occur due to losses or gains from radiation, and from fluxes through and stresses on the surface of the computational volume. With shearing-periodic boundary conditions, the net rate of change should ideally obey

$$\frac{d}{dt} \langle \mathcal{H} \rangle = q\Omega \left\langle \rho v_x \delta v_y - \frac{B_x B_y}{4\pi} \right\rangle + \langle -\rho \mathcal{L} \rangle. \quad (6)$$

Thus, if quasi-steady state is reached, we would then expect $d\langle \mathcal{H} \rangle / dt = 0$, and the sum of stresses times $q\Omega$ to equal the cooling rate. In steady state, from equation (3) the total rate of work done by the combination of compressions and shocks, $\langle -P \nabla \cdot \mathbf{v} \rangle + \langle \left(\frac{\partial \mathcal{E}}{\partial t} \right)_{shocks} \rangle$, plus any other dissipation, should also be balanced by the net cooling, $\langle \rho \mathcal{L} \rangle$.

In the upper panel of Figure 17 we plot (for our another realization of our standard run) the rate of work done by Reynolds and Maxwell stresses per unit volume. The late-time volume-averaged energy inputs from Maxwell and Reynolds stresses are 3.7 and 0.6 (in units of $P_0\Omega/2\pi$). The Maxwell stress dominates the Reynolds stress, which is typical in simulations of the MRI. In the lower panel of Figure 17 we plot the volume averaged shock heating, radiative heating - cooling rates, $-\langle \rho \mathcal{L} \rangle$, and pressure work, $-\langle P \nabla \cdot \mathbf{v} \rangle$, as a function of time. The sum of these three terms is approximately zero during the first few orbits of the simulation. Later in the simulation there is typically either net heating or cooling at any particular time, but the late time averages - individually, 1.0, -0.7, and -0.3 (in units of $P_0\Omega/2\pi$) for shock, radiation, and pressure terms - sum to zero. Thus, on average, radiative losses exceed radiative gains, cooling by rarefactions exceeds heating by compressions, and together these net loss terms balance gains in shocks. The mean energy density typically varies by 10% during the latter half of the simulation.

If total energy were perfectly conserved, as noted above, the energy inputs from Maxwell and Reynolds stresses would be balanced by net cooling. The energy source for this radiative cooling would, in turn, be provided by compressive work and dissipation of turbulence. The present simulation, however, in fact captures only part of the turbulent dissipation – that in shock heating, as mediated by artificial viscosity. In addition, both magnetic and kinetic turbulent energy are lost at the grid scale. Oppositely-directed magnetic fields and shear flows, when advected into a single zone, are averaged to zero. Since ZEUS evolves a (non-conservative) internal energy equation rather than a total energy equation, the associated energy from those small-scale sheared \mathbf{v} and \mathbf{B} fields is lost. In principle, these dissipation terms could be captured if explicit resistivity and shear viscosity were included.

3.7. Synthetic Line Profiles

Although the present simulations are highly idealized in many ways (e.g. they are vertically periodic rather than stratified), it is interesting to explore model properties that bear a close relation to observables. The profiles of 21 cm HI absorption directly trace the density, temperature, and turbulent velocities of the atomic ISM via a line-of-sight convolution. Using our simulated “data,” we can generate analogous maps of line profiles projected in any direction through the computational volume. Figures 18, 19, and 20 show synthetic emission profile maps for our standard model along the x, y, and z directions. We also present, paired with each line-of-sight velocity profile, the corresponding distribution of total emission with line-of-sight position. Each of the 8×8 windows on the map represents a volume of $32 \times 32 \times 256$ zones, integrated over the projected area. For each zone, the contribution to emission is proportional to the density, with a Gaussian velocity distribution centered on the flow velocity, and dispersion = $\sqrt{kT/\mu}$. Strong lines indicate more total mass along a given line of sight, and weak lines indicate less mass. Since most of the mass in our standard model is in the cold phase, a strong line indicates the presence of cold, dense gas.

For Figures 18, 19, and 20 the mean line widths of the velocity profiles are 1.8, 1.9, and 1.7 km s^{-1} . Without thermal broadening the line widths are reduced to 1.0, 1.3, and 0.7 km s^{-1} , which is consistent with the time-averaged velocity dispersions in the radial, azimuthal, and vertical directions reported in §3.4. Most of the velocity profiles are single-peaked, and would likely be interpreted as arising from one to three emitting components if a standard Gaussian fitting procedure were applied. However, our results show that in many cases several spatially-separated components are distinctly evident in the line-of-sight mass distributions. Velocity profile broadening and skewness statistically give evidence that more than one component is present, but we find no correlation between increased spatial coherence and increased velocity profile symmetry in any given direction. We do not observe any structure which shows two distinct lines. The absence of velocity profiles with two distinct peaks owes in part to the thermal broadening, which smears out smaller scale features. However, the primary reason that profiles are single-peaked is that velocity modes at a large range of wavenumbers are present in saturated state MRI-driven turbulence. Since there is no single dominant wavelength along the line-of-sight, the range of velocities is smoothly filled.

The spatial resolution of the synthetic observations was doubled to determine if the structure of the velocity profiles would be affected. Generally, the line profiles remain single-peaked, whether or not well-separated spatial components are present. In Figure 21 we show velocity profiles for the warm gas only, and do not include thermal broadening. The

line-of-sight position profile (also in Figure 21) shows that the warm gas is spatially much more uniformly distributed than the cold gas, which dominates the profiles in Figures 18 - 20. Interestingly, however, the intermediate-temperature gas is always associated with cold condensations. This is clearly seen in Figure 22, which shows slices through the volume both before and after the onset of strong turbulence.

The line profiles for runs with different mean density are very similar to the standard run. They typically show a single component with occasional evidence for a weaker second component. As the mean density is decreased to $n = 0.67$ and 0.25 cm^{-3} , the line widths increase to 2.0 , 2.2 , and 1.9 km s^{-1} , and 4.8 , 4.7 , and 4.5 km s^{-1} , respectively. Without thermal broadening the line widths are reduced to 1.1 , 1.5 , and 0.74 km s^{-1} , and 2.2 , 2.2 , and 1.1 km s^{-1} , respectively. A similar trend of decreasing line width with increasing mean density is also observed.

4. Summary and Discussion

In this paper, we present results from a set of numerical MHD simulations that focus on the interrelationship between turbulence and thermal structure. The models we have performed are three dimensional, and include sheared galactic rotation and magnetic fields. Turbulence therefore is generated by the magnetorotational instability. We also include a radiative cooling function that, in pressure equilibrium, would yield a two-phase medium. The two fundamental issues we have addressed are (1) how cloudy structure alters the saturated-state properties and scalings of MRI-driven turbulence, compared to single-phase MRI models, and (2) how turbulence that is *not* driven by direct (stellar) thermal energy inputs affects the thermal balance and phase structure in the warm/cold atomic medium.

4.1. Summary of Model Results

Our primary findings are as follows:

1. *Evolution and physical structure:* A two-phase cloudy medium with many small clouds develops in the first 20 Myr of our simulations. Over time, due initially to galactic shear, and later ($t > 5$ orbits) to MRI-driven turbulence, these clouds undergo a continual series of mergers and disruptions, leading to a late-time state in which the mass function of condensations peaks at a few hundred M_\odot . The dense condensations are triaxial, and typically have max:min axis ratios of 2:1. They consist of cold gas lumps surrounded by envelopes of thermally-unstable gas; filling all of the remaining volume is thermally-stable

warm gas.

2. *Density and temperature distributions:* For the range of parameters we have explored, in late stages of evolution most of the gas mass is in the cold phase, while most of the volume is occupied by the warm phase. While the proportion of thermally-unstable intermediate-temperature gas in a given model increases after the advent of MRI, at all stages the density and temperature PDFs show distinct warm and cold phases, with a varying amount of material in the “non-equilibrium” valley between these peaks. The peaks, near $T = 100$ K and $T = 8000$ K, also broaden as the turbulence develops. The relative proportions in each phase depend on the mean density, varying from 95% cold gas when the mean density $\bar{n} = 4.0 \text{ cm}^{-3}$, to 50% cold gas when $\bar{n} = 0.25 \text{ cm}^{-3}$. The fractions of thermally-unstable gas and warm gas are always comparable to each other. Increasing levels of turbulence yield increasing proportions of thermally-unstable gas. Relative to the proportions predicted for a two-phase, quiescent medium in thermal and pressure equilibrium, increasing turbulence also tends to *increase* the fraction of cold gas, while decreasing the fraction of warm stable gas.

3. *Pressure:* We initialize our models at $P/k = 2000 \text{ K cm}^{-3}$, but secular cooling in the stages before MRI develops leaves the gas in approximate pressure equilibrium ($\Delta P/\bar{P} < 0.1$) at a lower mean pressure of $P/k = 1300 \text{ K cm}^{-3}$, near the minimum for which two stable gas phases can be present. After MRI develops, pressures cover a much wider range of values ($\Delta P/\bar{P} \sim 0.5$), with a maximum at $P/k \sim 4000 \text{ K cm}^{-3}$, but relatively unchanged mean value ($\bar{P}/k = 1200 \text{ K cm}^{-3}$).

4. *Turbulent velocities:* After the MRI saturates at ~ 5 orbits, the turbulent velocity dispersion reaches a quasi-steady plateau – albeit with fluctuations of $\sim 30\%$ in amplitude. For our fiducial model with $\bar{n} = 1 \text{ cm}^{-3}$, the mean late time (3D) velocity dispersion is $\delta v \equiv \langle v_x^2 + (\delta v_y)^2 + v_z^2 \rangle^{1/2} \approx 2.7 \text{ km s}^{-1}$ for all three components. This velocity corresponds to mean Mach numbers of 0.4, 1.8 and 2.9 in the warm, intermediate, and cold phases. We examined the effect of mean density on the velocity dispersion, and found that $\delta v \propto \bar{n}^{-0.77}$ overall, with slightly shallower slope for the warm gas alone. Our results show, additionally, that the Reynolds stress, $\langle \rho v_x \delta v_y \rangle$, varies with mean density $\propto \bar{n}^{-1.1}$. We find that the in-plane components of the velocity dispersion exceed the component perpendicular to the disk by about a factor of two.

5. *Magnetic fields:* For the present set of models, we have adopted initial conditions with a uniform vertical magnetic field of strength $0.26 \mu\text{G}$. The MRI enhances the field by an order of magnitude, so that $\langle B^2 \rangle^{1/2}$ is typically $2 - 3 \mu\text{G}$ late in the simulation. The field strength is similar (within $\sim 20\%$) in all three phases of gas, and there is no significant trend of field strength with mean simulation density \bar{n} . However, we find that the Maxwell stress,

$\langle -B_x B_y / (4\pi) \rangle$, varies with mean density $\propto \bar{n}^{-0.4}$.

6. *Synthetic line profiles*: As a demonstration of the potential for employing simulations to interpret observational diagnostics, we have computed maps of synthetic line profiles from sample data cubes. We find that the line profiles are generally single-peaked (although in some cases would require two or three components if a standard Gaussian fitting scheme were performed). In no case did we identify two distinct velocity components, even though there are distinct cloud structures present along many lines of sight. Because turbulence has a smooth power spectrum, this kind of overlap in velocity space is inevitable.

Our results have several interesting implications for interpreting ISM observations, and it is also interesting to compare with recent numerical and theoretical work on the ISM and on MRI dynamics. We conclude by discussing these connections.

4.2. The Multiphase MRI and Saturated-State Turbulence

High levels of turbulence are observed both in the atomic gas of the Milky Way, and in that of external spiral galaxies, and it has been suggested that the MRI could be an important contributor to this turbulence, especially in the outer parts of galaxies where there is little star formation. Our models are the first (to our knowledge) to address this issue directly with an appropriate physical model – namely, one that admits two stable thermal phases, such that the MRI must develop in a cloudy medium with density contrasts of 100 between clumps and diffuse gas. While the turbulent velocity that develops in our fiducial model with mean density $\bar{n} = 1 \text{ cm}^{-3}$ is relatively modest, the scaling of the turbulent amplitude with \bar{n} is quite steep, such that $\delta v \sim 8 \text{ km s}^{-1}$ is predicted when $\bar{n} = 0.2 \text{ cm}^{-3}$.

The scaling of turbulent velocity dispersion with mean density indicates that MRI may play a significant role in the outer regions of the galaxy. Beyond the point in the Milky Way where the stellar surface density drops, the gas scale height rapidly increases, and the volume density correspondingly decreases; this sort of disk flaring is also seen in external galaxies. In the Wolfire et al. (2003) Milky Way model, for example, \bar{n} falls below 0.2 cm^{-3} at $R = 15 \text{ kpc}$. The outer-galaxy pressure in the Wolfire et al. (2003) model is nevertheless high enough for cold-phase gas to be present, so that if it were *not* turbulent, then a thin gravitationally unstable layer would develop.¹ Our results suggest that the MRI could be maintaining high-

¹For a cold layer without turbulence, the value of the Toomre Q is < 1.5 (the threshold for instability) for $R\Sigma > 12 \text{ kpc} \times 1M_\odot \text{ pc}^{-2}$, where Σ is the gas surface density. Wolfire et al. (2003) show that cold gas is expected to be present at all radii out to 18 kpc. Since Σ is estimated to exceed $3M_\odot \text{ pc}^{-2}$ inside this radius, even if only 20% of the gas is in the cold component, the layer would be gravitationally unstable.

amplitude turbulence, and hence suppressing star formation, in the far outer Milky Way and other spiral galaxies. We note that the increase in scale height is necessary for this to hold; since the minimum MRI wavelength $\propto \bar{n}^{-1}$, MRI-driven turbulence can only be sustained in a sufficiently thick disk.

Even in the inner disk, our results suggest that MRI may be a significant contributor to turbulence in the ISM. At a mean inner-Galaxy ($R < 10$ kpc) midplane density of $\bar{n} = 0.6$ cm $^{-3}$ (Dickey & Lockman 1990; Wolfire et al. 2003), our results would predict $\delta v \approx 4$ km s $^{-1}$. Away from the midplane where the density drops, the turbulent amplitudes would increase. The mean inner-disk vertical magnetic field strength may also be somewhat larger than the fiducial value we have adopted (Han, Manchester, & Qiao (1999) obtained $\langle B_z \rangle = 0.37$ μ G from pulsar observations), which would tend to increase the amplitude of the turbulence. A more extensive parameter survey – allowing for disk stratification, varying scale height, and differing initial field strengths and distributions – is needed to quantify more fully the expected contribution from MRI to turbulent amplitudes in the ISM. Another important question is whether MRI development could be quantitatively altered by interaction with large-scale perturbations driven by supernovae or spiral shocks. We defer consideration of this interesting issue to future work.

Direct comparisons between simulations and observations regarding levels of turbulence and magnetic field strength as a function of local parameters would be very useful. Unfortunately, observations at this time do not permit such comparisons to be made. HI velocity dispersions in the Milky Way can only be measured within ~ 1 kpc of the Sun (e.g. Lockman & Gehman (1991); Heiles & Troland (2003)). In external near-face-on galaxies, observed (vertical) velocity dispersions combine both turbulent and thermal contributions, and these values do not vary secularly with galactic radii (although dispersions are significant) even well beyond the optical disk (see §1). Magnetic field strengths in the Milky Way beyond ~ 10 kpc have not been measured directly (i.e. with Faraday rotation; see e.g. Han, Ferriere, & Manchester (2004)). For both the Milky Way and external galaxies, one may use synchrotron emission (Beck 2004) to obtain the product of the magnetic and cosmic ray energy densities as a function of galactic radius, but since the equipartition assumption need not be satisfied everywhere, this does not yield a B-field strength except locally, where electron cosmic-ray and gamma-ray observations can be made. Milky Way outer-galaxy field strengths of 2-3 μ G are consistent with synchrotron/cosmic ray models of Strong, Moskalenko, & Reimer (2000).

The scalings we find for MRI amplitudes show interesting differences from those obtained with single-phase gaseous media, in previous adiabatic and isothermal simulations. In the shearing-box models of HGB1, HGB2, and Sano et al. (2004), all of the measures of turbu-

lence scale together – i.e. $\langle B^2 \rangle \propto \langle -B_x B_y \rangle \propto \langle \rho(\delta v)^2 \rangle \propto \langle \rho v_x \delta v_y \rangle$. For simulations with net vertical magnetic flux, HGB1 further reported that these stresses and energy densities scale $\propto L_z \Omega v_{A,z} / c_s^2$, where $v_{A,z}$ and c_s are the initial Alfvén speed and sound speed, respectively. Sano et al. (2004), on the other hand, identify a scaling of stresses $\propto v_{A,z}^{3/2}$ in the mean Alfvén speed, and also demonstrate that the pressure dependence of the saturated-state stresses are very weak.

While we have not surveyed cases with differing magnetic field strengths, our models at varying mean density have varying $v_{A,z}$. At fixed mean B_z , the single-phase medium simulations cited above would predict scalings $\propto \bar{n}^{-1/2}$ or $\propto \bar{n}^{-3/4}$ for $\langle B^2 \rangle$, $\langle \rho(\delta v)^2 \rangle$, and the stresses. For our cloudy-medium simulations, we in fact find that $\langle B^2 \rangle$ is nearly independent of \bar{n} , while other scalings in our models are either in the same range as the single-phase predictions (i.e. $\langle \rho(\delta v)^2 \rangle \propto \bar{n}^{-0.54}$ and $\langle -B_x B_y \rangle \propto \bar{n}^{-0.4}$), or slightly steeper ($\langle \rho v_x \delta v_y \rangle \propto \bar{n}^{-1.1}$). Interestingly, 3D MRI simulations in radiation-dominated disks (Turner et al. 2003), which like our models contain strong density contrasts, also show a steep dependence of the stress $\propto v_{A,z}^2$.

The reason for the difference between single-phase and cloudy-medium results for saturated-state $\langle B^2 \rangle$ scalings is not yet clear, but the lack of dependence on \bar{n} in our models suggests that local, rather than global, properties of the gas determine the field strength that develops. The densities in the diffuse phase and in the dense phase are similar for all our models; only the filling factor of cold clouds differs appreciably. If the saturated-state field strength depends on the reconnection rate, and this depends on local gas densities and field geometry, then the fact that these properties are the same in all our two-phase models might explain the lack of dependence of $\langle B^2 \rangle$ on \bar{n} . Our isothermal model, which has less-kinked magnetic field, and typical (log) densities midway between $\log(n_{warm}) \sim -1$ and $\log(n_{cold}) \sim 1$, indeed has saturated-state values of the RMS field strength 20-50% higher than the standard run ($3.5 \mu\text{G}$ in the isothermal model, compared to 2.4 , 2.7 , and $2.9 \mu\text{G}$ in the F, G, and H phases for the standard run). Further study, with particular focus on the rate and spatial distribution of reconnection, is needed to clarify this issue.

While the saturated-state magnetic field strength depends on a balance between MRI-driven amplification and (numerical or true resistive) dissipation, the saturated-state velocity dispersion depends on a balance between MRI driving and losses in shocks, compressions, and (numerical or true viscous) shear dissipation. Since turbulent velocities are similar in all the gas components, while the mass is concentrated in the cold clouds, in Paper I we proposed that the cloud collision time may be a good proxy for the kinetic energy dissipation time. The kinetic energy dissipated per unit time per unit mass is then $\dot{\mathcal{E}}_{diss} \sim (\delta v)^3 \bar{\rho} / (r_{cl} \rho_{cl})$, where r_{cl} is a cloud size and $\rho_{cl} \approx \rho_{cold}$ is the gas density within clouds. The kinetic energy input

rate per unit mass due to MRI is an order-unity constant times $\Omega \langle -B_x B_y \rangle / (4\pi\bar{\rho})$. Balancing inputs with dissipation, and using $\langle -B_x B_y \rangle \propto \bar{\rho}^{-0.4}$ from our simulations, this predicts a scaling for the saturated-state velocity dispersion $\delta v \propto \bar{\rho}^{-0.8}$. This prediction indeed agrees well with the velocity dispersion scaling measured directly from our simulations, $\delta v \propto \bar{\rho}^{-0.77}$. Of course, this scaling cannot continue to arbitrarily low density, because the MRI becomes stabilized if the wavelength ($\propto 1/\sqrt{\bar{\rho}}$) exceeds the height of the disk.

In previous analytic work on magnetized cloud-cloud collisions Clifford & Elmegreen (1983) argued that effective cloud cross sections should vary $\propto (\bar{\rho}\delta v)^{-2/3}$. Although we do not measure this effect directly, it would not be expected to change our results significantly. Taking this into account for r_{cl} in the above analysis, the predicted power-law scaling exponent for δv with $\bar{\rho}$ changes by only 0.02.

4.3. Structure and Thermodynamics of the Atomic ISM

As noted above, our results show only minor differences between typical magnetic field strengths in gas of different phases, with the cold medium having slightly higher B . If flux were frozen to the gas, and cold clouds contracted isotropically out of the warm ISM due to TI, then the field strengths would differ by a factor 20 between diffuse and dense phases. Evidently, however, this is not the case: observationally, Heiles (2004) reports the B -fields in cold atomic clouds are no stronger than in the diffuse ISM overall. Our models are consistent with this result, in part because clouds in fact do not condense isotropically (but instead preferentially gather material along field lines), and in part because field lines can diffuse relative to matter (in our models, this is purely numerical, but turbulent diffusion is likely to play the same physical role).

Synthetic line profiles of the sort we have computed are potentially of great value in interpreting observations of the ISM, and in particular, the emission and absorption profiles of the 21 cm hydrogen line. Ensemble properties of the atomic ISM, including the turbulent velocity dispersion for the cold gas separately, can be unambiguously obtained from observed position-velocity data cubes. Our results illustrate the difficulty, however, in discerning detailed (local) structural properties of the ISM directly from line profiles, due to overlapping in velocity space (cf. Ostriker, Stone, & Gammie 2001). Fortunately, recent work has demonstrated that analysis techniques calibrated using simulations can be used to extract fundamental statistical properties such as power spectra from CO observations of turbulent molecular clouds (e.g. Brunt et al. (2003); Heyer & Brunt (2004)), and it will be interesting to test whether the same holds true for HI gas.

What do we conclude regarding the dynamics/thermodynamics connection in the turbulent atomic ISM? As alluded to in §1, recent observations (Heiles & Troland 2003) have suggested that at least 30% of the HI gas at high latitudes (where blending due to galactic rotation is minimized) is in the thermally-unstable regime ($T = 500 - 5000$ K). Another 30% of the HI mass at high latitudes is estimated to be warm, thermally-stable gas.² Interestingly, we find that in our simulations, the warm and thermally-unstable gas mass fractions are also always very similar. In our models, the warm+unstable mass fraction only approaches 50% for the lowest- \bar{n} case; at $\bar{n} = 0.67\text{cm}^{-3}$, the warm+unstable gas comprises 30% of the total mass. However, except at the lowest \bar{n} , the turbulent amplitudes in our models are also somewhat lower than in the real ISM, so in part the lower warm+unstable fractions we find may owe to lower rates of turbulent dissipation. In addition, as discussed in §3.6, because our numerical method is non-conservative, a significant fraction of the input turbulent energy from the MRI is lost without being thermalized. Our method therefore underestimates the heating rate. This may be especially true in high density regions where the magnetic field curvature is large, so that the current density $\mathbf{J} = \nabla \times \mathbf{B}$ is large, and the resistive heating $\propto |\mathbf{J}|^2$ should also be large. We intend to explore this issue in future work incorporating explicit resistivity, also comparing with results using a conservative algorithm to update the energy equation.

Overall, our results are consistent with the recent work of Audit & Hennebelle (2004), who performed high resolution 2D simulations of a converging flow in which turbulence develops, using a cooling function very similar to ours. The temperature and density PDFs from their models are qualitatively similar to ours, in particular showing evidence for the existence of a two-phase medium even in the most turbulent case. Similar to our results, they found that the proportion of thermally-unstable gas increases with the amplitude of turbulence. For their least turbulent model, about 10% of the gas was thermally unstable, while this fraction increased to 30% in models with larger turbulent amplitudes.

Other recent work, based on simulations that include modeled effects of star formation via prescriptions for OB star heating (e.g. Vázquez-Semadeni, Gazol, & Scalo (2000); Gazol et al. (2001); Vázquez-Semadeni et al. (2003)) and supernovae (e.g. Rosen & Bregman (1995); Korpi et al. (1999); de Avillez (2000); Wada, Spaans, & Kim (2000); Wada & Norman (2001); Wada (2001); Balsara et al. (2004); Mac Low et al. (2004)), have found significant fractions of gas in the unstable phase, and many have advocated for a shift away from the classical two- or three-phase medium concept towards more of a “phase continuum”

²At low latitudes, however, there is a very strong peak in the total gas column at $T \approx 8000 - 9000$ K in the Heiles & Troland (2003) data, suggesting that midplane gas may be much more likely to be in thermal equilibrium.

description. However, the former set of models have energy inputs from “star formation” in cold atomic gas (rather than in self-gravitating molecular clouds), which likely leads to overestimating the amount of thermally-unstable gas. The latter models have not included low-temperature cooling, so no cold phase can form. Thus, it is not yet clear whether realistic models incorporating turbulence driven by star formation would indeed produce an extended, featureless continuum of temperatures, or whether they would yield bimodal distributions similar to those we have found with solely MRI-driven turbulence.

We believe that, given the observed turbulent amplitudes ($\sigma_v \sim 10 \text{ km s}^{-1}$) and characteristic spatial scales (the disk thickness $H \sim 100 \text{ pc}$) for the atomic ISM, quasi-two-phase distributions are inevitable. The heating time $\sim H/\sigma_v = 10^7 \text{ yr}$ is a factor of a few longer than the cooling time in gas at densities $\lesssim 1 \text{ cm}^{-3}$ (see eq. [5] of Paper I or eq. [4] of Wolfire et al. (2003)), so that moderate but not extreme departures from thermal equilibrium can be expected in diffuse gas. In dense gas, cooling times are very short, so thermal equilibrium must hold, but typical order-unity variations in pressure from sonic-level turbulence can lead to moderate local density and temperature variations. Future work will be able to determine whether, with realistic turbulent amplitudes and fully-captured energy dissipation, thermal distributions from models can indeed match those from HI observations, or whether additional heat sources are required.

We are grateful to Charles Gammie, Woong-Tae Kim, Jim Stone, and Mark Wolfire for valuable discussions, and Yen-Ting Lin and Jonathan McKinney for helpful technical advice. The manuscript has also benefited from a thoughtful and detailed report prepared by an anonymous referee. This work was supported in part by grants NAG 59167 (NASA) and AST 0205972 (NSF). Some of the computations were performed on the Tungsten cluster at NCSA, and others were performed on the CTC cluster in the UMD Department of Astronomy.

REFERENCES

Audit, E. & Hennebelle, P. 2004, *astroph*-0410062

Balsara, D.S., Kim, J., Mac Low, M., & Mathews, G.J. 2004, *ApJ*, 617, 339

Beck, R. 2004, *Astrophys. & Sp. Sci.*, 289, 293

Brunt, C.M., Heyer, M.H., Vázquez-Semadeni, E., & Pichardo, B. 2003, *ApJ*, 595, 824

Burkert, A. & Lin, D.N.C 2000, *ApJ*, 537, 270

Clifford, P. & Elmegreen, B.G. 1983, MNRAS, 202, 629

Heyer, M.H. & Brunt, C.M. 2004, ApJ, 615, L45

de Avillez, M.A. 2000, MNRAS, 315, 479

de Avillez, M.A. & Breitschwerdt, D. 2005, MNRAS, astroph-0502327

Dickey, J.M., Hanson, M.M., & Helou, G. 1990, ApJ, 352, 522

Dickey, J.M. & Lockman, F.J. 1990 ARA&A, 28, 215

Dziourkevitch, N., Elstner, D., & Rüdiger, G. 2004, A&A, 423, 29

Hawley, J. F. & Evans, C.R. 1988 ApJ, 332, 659

Elmegreen, B.G., Scalo, J. 2004, ARA&A, 42, 211

Field, G.B. 1965 ApJ, 142, 531

Field, G.B., Goldsmith, D.W., & Habing, H.J. 1969, ApJ, 155, 149

Gammie, C.F., Lin, T., Stone, J.M., & Ostriker, E.C. 2003, ApJ, 592, 203

Gazol, A., Vázquez-Semadeni, E., Sánchez-Salcedo, F.J., & Scalo, J. 2001, ApJ, 557, L121

Hawley, J.F., & Stone, J.M. 1995 Computer Physics Communications, 89, 127

Hawley, J.F. & Balbus, S. A. 1992, ApJ, 400, 595

Hawley, J.F., Gammie, C.F., & Balbus, S.A., ApJ, 440, 742 (HGB1)

Hawley, J.F., Gammie, C.F., & Balbus, S.A., ApJ, 464, 690 (HGB2)

Han, J.L., Ferriere, K., & Manchester, R.N. 2004, ApJ, 610, 820

Han, J.L., Manchester, R.N., & Qiao, G.J. 1999, MNRAS, 306, 371

Heiles, C. & Troland, T.H. 2003, ApJ, 586, 1067

Heiles, C. 2004, in Star Formation In the Interstellar Medium eds. D. Johnstone, F.C. Adams, D.N.C. Lin, D.A. Neufeld and E.C. Ostriker (ASP:San Francisco, p. 79)

Hennebelle, P. & Péroult, M. 1999, A&A, 351, 309

Kim, W., Ostriker, E.C., & Stone, J.M. 2002, ApJ, 581, 1080

Kim, W., Ostriker, E.C., & Stone, J.M. 2003, ApJ, 599, 1157

Korpi, M.J., Brandenburg, A., Shukurov, A., Tuominen, I., & Nordlund, Å. 1999, ApJ, 514, L99

Koyama, H. & Inutsuka, S. 2002, ApJ, 564, L97

Kritsuk, A.G. & Norman, M.L. 2002a, ApJ, 569, L127

Kritsuk, A.G. & Norman, M.L. 2004, ApJ, 601, L55

Lockman, F.J. & Gehman, C.S. 1991, ApJ, 382, 182

Mac Low, M., Balsara, D., Kim, J., & Avillez, M.A. 2004, astroph-0410734

Mac Low, M. & Klessen, R.S. 2004, RevModPhys, 76, 125

McClure-Griffiths, N.M., Green, A.J., Dickey, J.M., Gaensler, B.M., Haynes, R.F., & Wieringa, M.H. 2001, ApJ, 551, 394

McKee, C.F. & Ostriker, J.P. 1977, ApJ, 218, 148

Mohan, R., Dwarakanath, K.S., & Srinivasan, G. 2004, astroph-0410627

Ostriker, E.C., Stone, J.M., & Gammie, C.F. 2001, ApJ, 546, 980

Petric, A. & Rupen, M.P. 2001, in Gas and Galaxy Evolution eds. J.E. Hibbard, M.P. Rupen, & J.H. van Gorkom (ASP:San Francisco), p. 288

Piontek, R.A. & Ostriker, E.C. 2004, ApJ, 601, 905, (Paper I)

Rosen, A. & Bregman, J.N. 1995, ApJ, 440, 634

Sánchez-Salcedo, F.J., Vázquez-Semadeni, E., & Gazol, A. 2002, ApJ, 577, 768

Sano, T., Inutsuka, S., Turner, N.J., & Stone, J.M. 2004, ApJ, 605, 321

Sellwood, J.A. & Balbus, S.A. 1999, ApJ, 511, 660

Slyz, A., Devriendt, J., Bryan, G., & Silk, J. 2004, astroph-0411383

Spitzer, L., Jr. 1978, Physical Processes in the Interstellar Medium (New York:Wiley)

Stone, J. M., Hawley, J.F, Gammie, C.F, & Balbus, S.A. 1996, ApJ, 463, 656

Stone, J. M. & Norman, M. L. 1992a, ApJ, 80, 753

Stone, J. M. & Norman, M. L. 1992b, *ApJ*, 80, 791

Strong, A.W., Moskalenko, I.V., & Reimer, O. 2000, *ApJ*, 537, 763

Taylor, A.R., et al. 2003, *AJ*, 125, 3145

Turner, N.J., Stone, J.M., Krolik, J.H., & Sano, T. 2003, *ApJ*, 593, 992

van Zee, Liese, & Bryant, J. 1999, *AJ*, 118, 2172

Vázquez-Semadeni, E., Gazol, A., & Scalo, J. 2000, *ApJ*, 540, 271

Vázquez-Semadeni, E., Gazol, A., Passot, T., Sánchez-Salcedo, J. 2003, in *Turbulence and Magnetic Fields in Astrophysics*, eds. E. Falgarone and T. Passot, (Berlin:Springer-Verlag) p. 213

Wada, K. & Norman, C.A. 2001a, *ApJ*, 547, 172

Wada, K., Spaans, M., & Kim, S. 2000, *ApJ*, 540, 797

Wada, K. 2001b, *ApJ*, 559, L41

Williams, J.P., de Geus, E.J., & Blitz, L. 1994, *ApJ*, 428, 693

Wolfire, M.G., Hollenbach, D., McKee, C.F., Tielens, A.G.G.M., & Bakes, E.L.O. 1995, *ApJ*, 443, 152

Wolfire, M.G., McKee, C.F., Hollenbach, D., & Tielens, A.G.G.M. 2003, *ApJ*, 587, 278

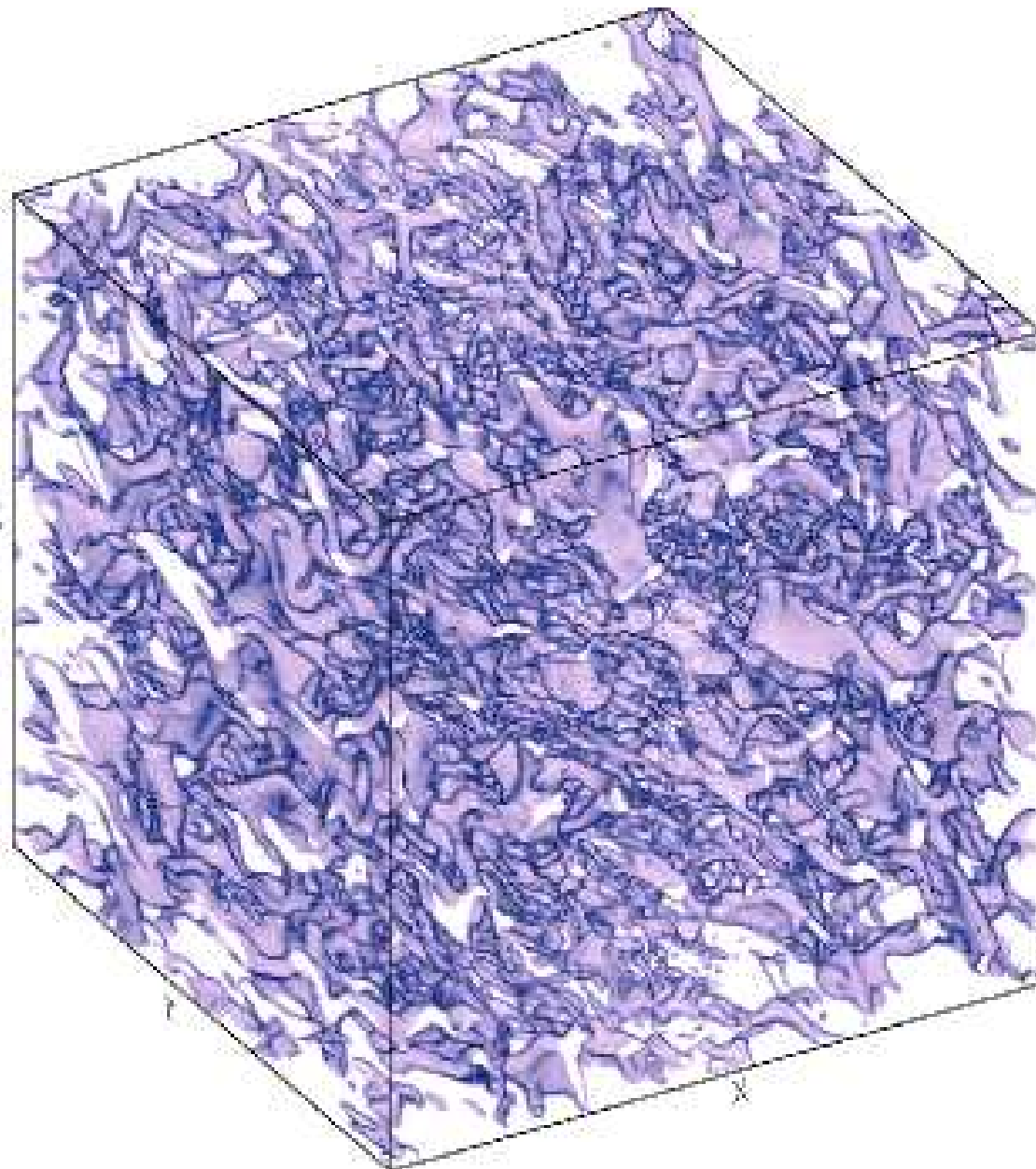


Fig. 1.— Volume rendering of density for the standard run at $t=1.0$ orbits. The “y” direction is azimuthal in this model, and the “x” direction is radial. Most of the mass is in the cold phase, while most of the volume is occupied by the warm phase.

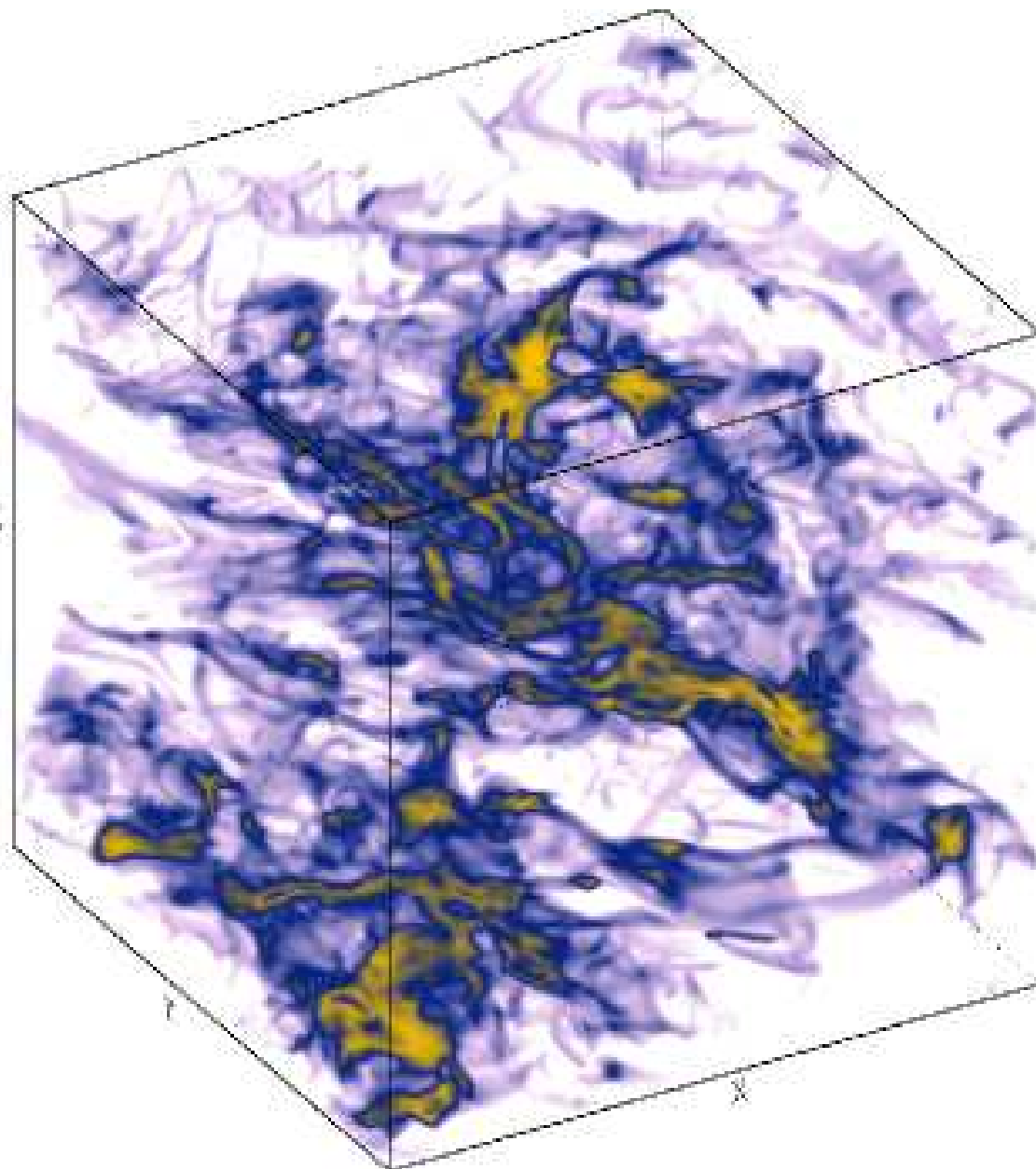


Fig. 2.— Volume rendering of density for the standard run at $t=9.0$ orbits. Turbulence due to the MRI has forced gas to higher densities, as well as increased the mass fraction of the unstable phase. Many filamentary structures are present.

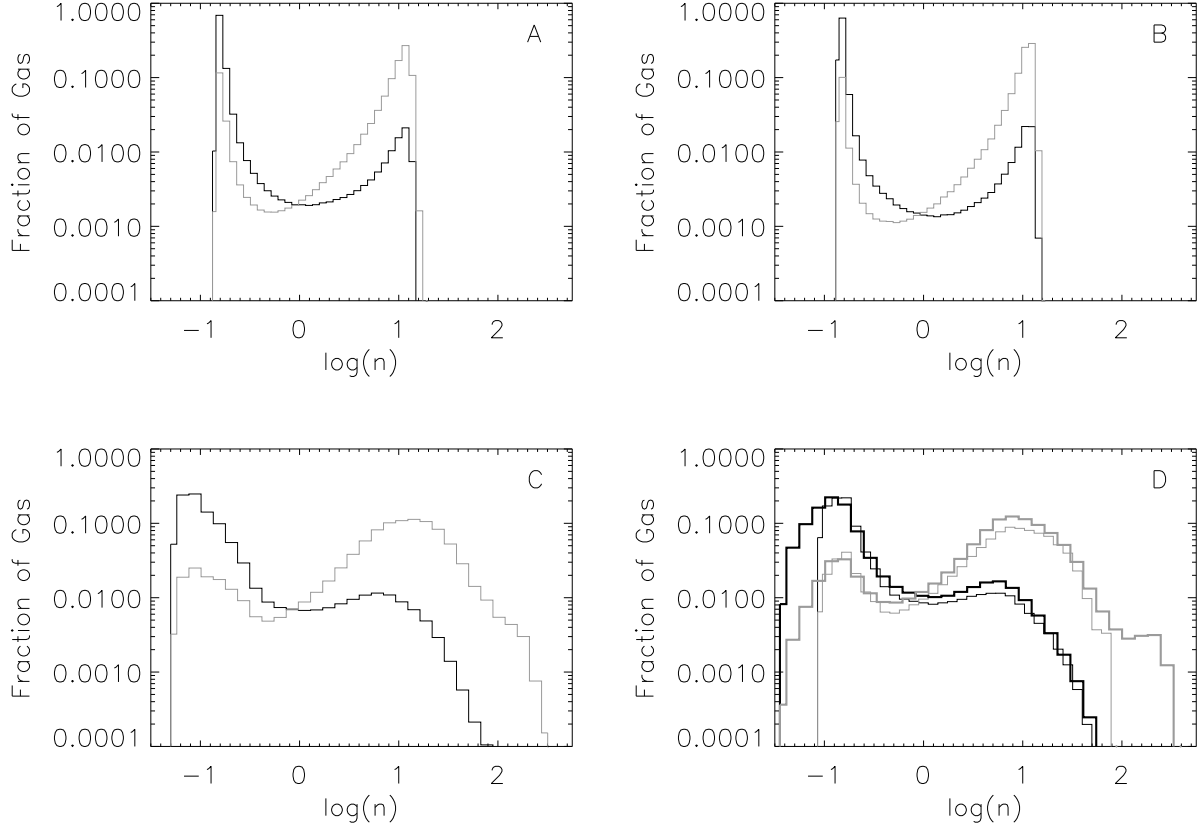


Fig. 3.— Volume (black line) and mass (grey line) PDFs of density for the standard run at $t = 1, 2.5$, and 5.0 orbits (panels A-C, respectively). In Panel D we compare the PDFs for our two resolutions of 128^3 (thin lines) and 256^3 (thick lines) at $t = 9$ orbits. The PDF changes little between Panels A and B. In Panels C and D the development of the MRI increases the fraction of gas in the unstable phase, and forces gas to higher densities. In Panel D, the higher resolution run contains trace amounts of gas at more extreme densities.

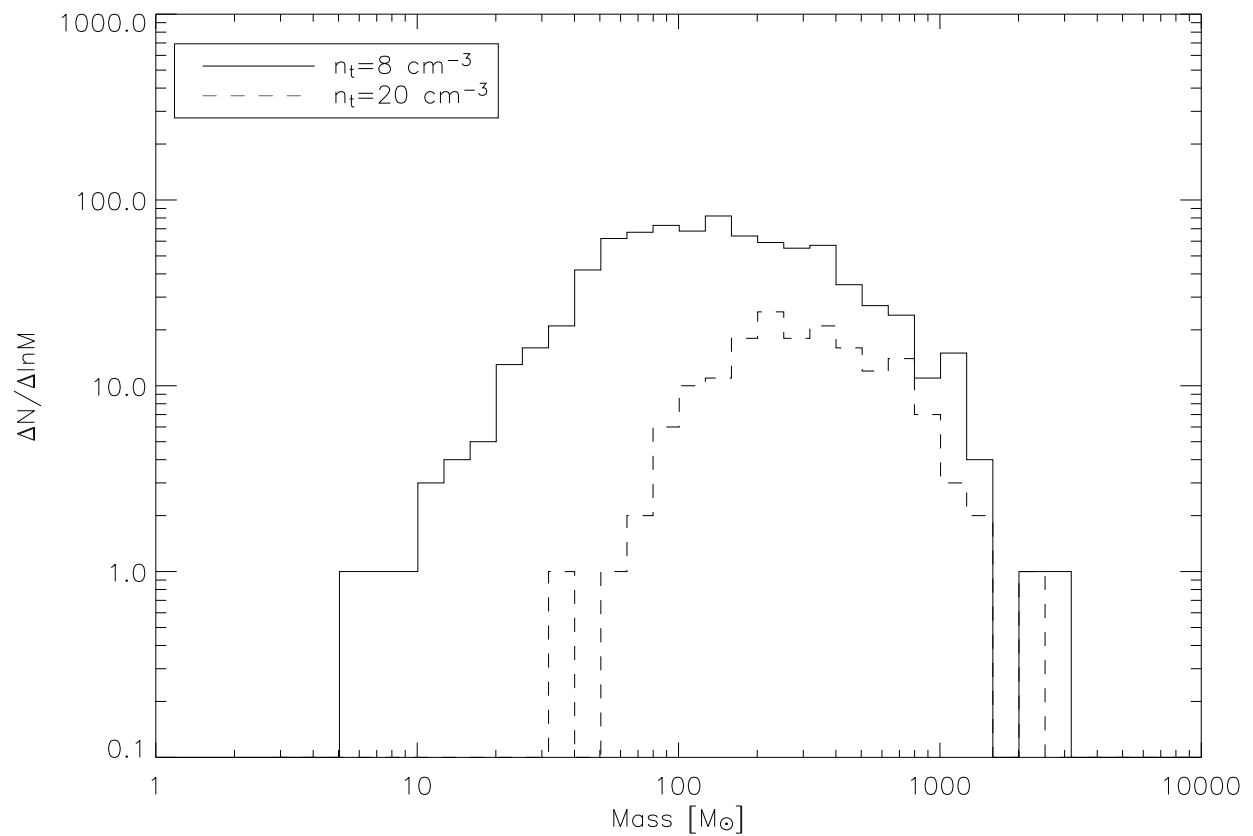


Fig. 4.— Mass spectrum of clumps from snapshot at $t = 6.5$ orbits, with threshold densities of 8 and 20 cm^{-3} .

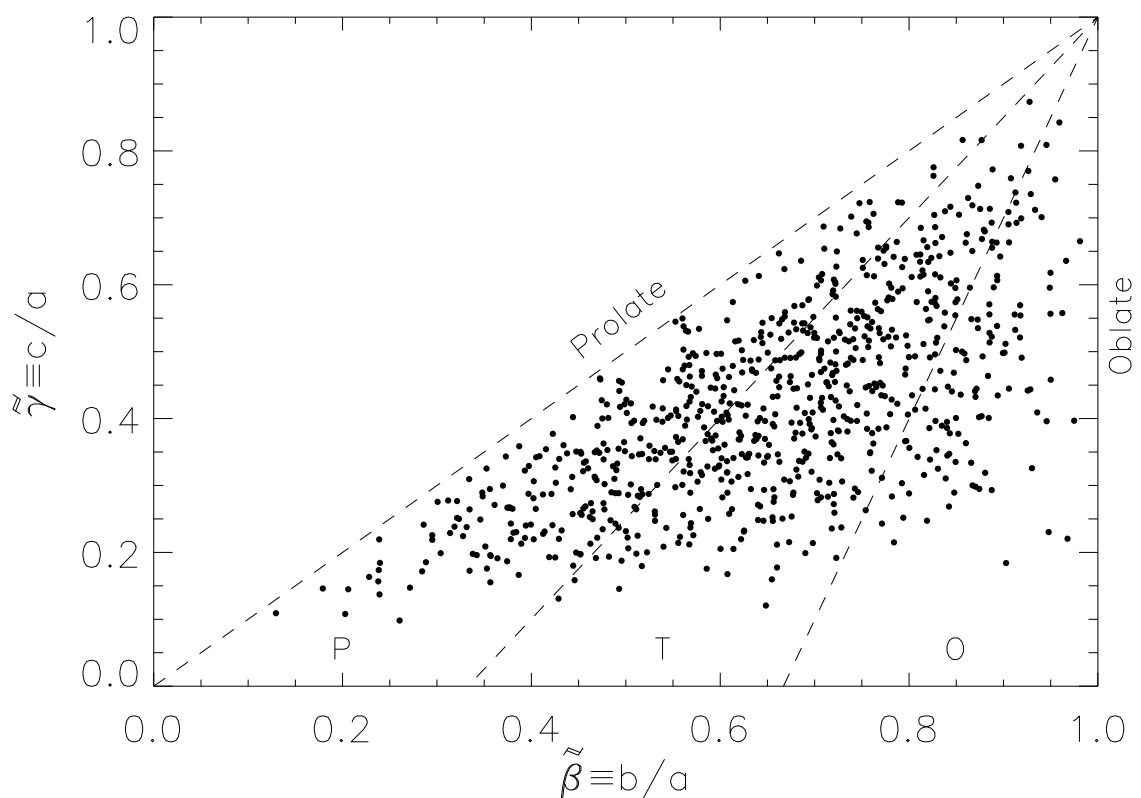


Fig. 5.— Axis ratios for clumps at $t = 6.5$ orbits, taking $n_t = 8 \text{ cm}^{-3}$.

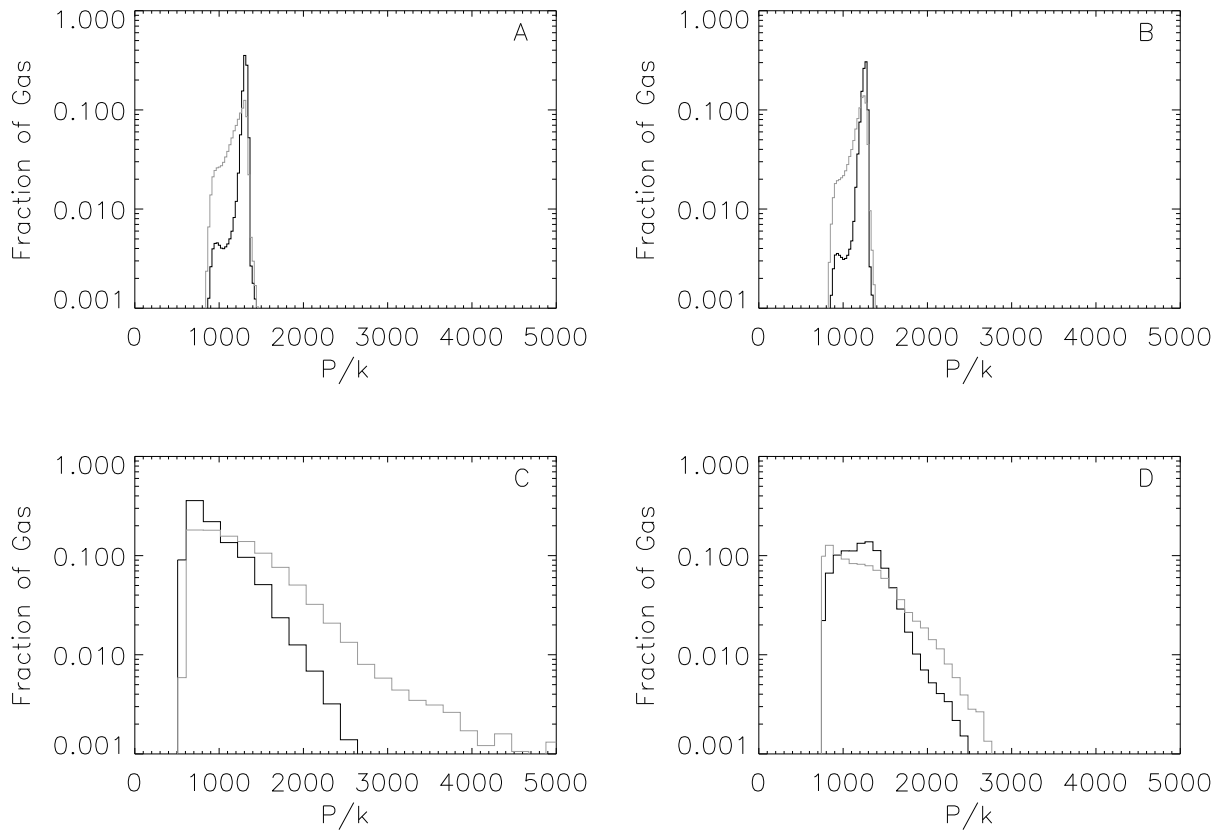


Fig. 6.— Volume (black line) and mass (grey line) PDFs of pressure for the standard run at $t = 1, 2.5, 5.0$, and 9 orbits (panels A-D, respectively). Early in the simulation most of the gas is found in the range of $P/k=900-1300 \text{ K cm}^{-3}$. The MRI has drastically altered the pressure distribution in Panels C and D.

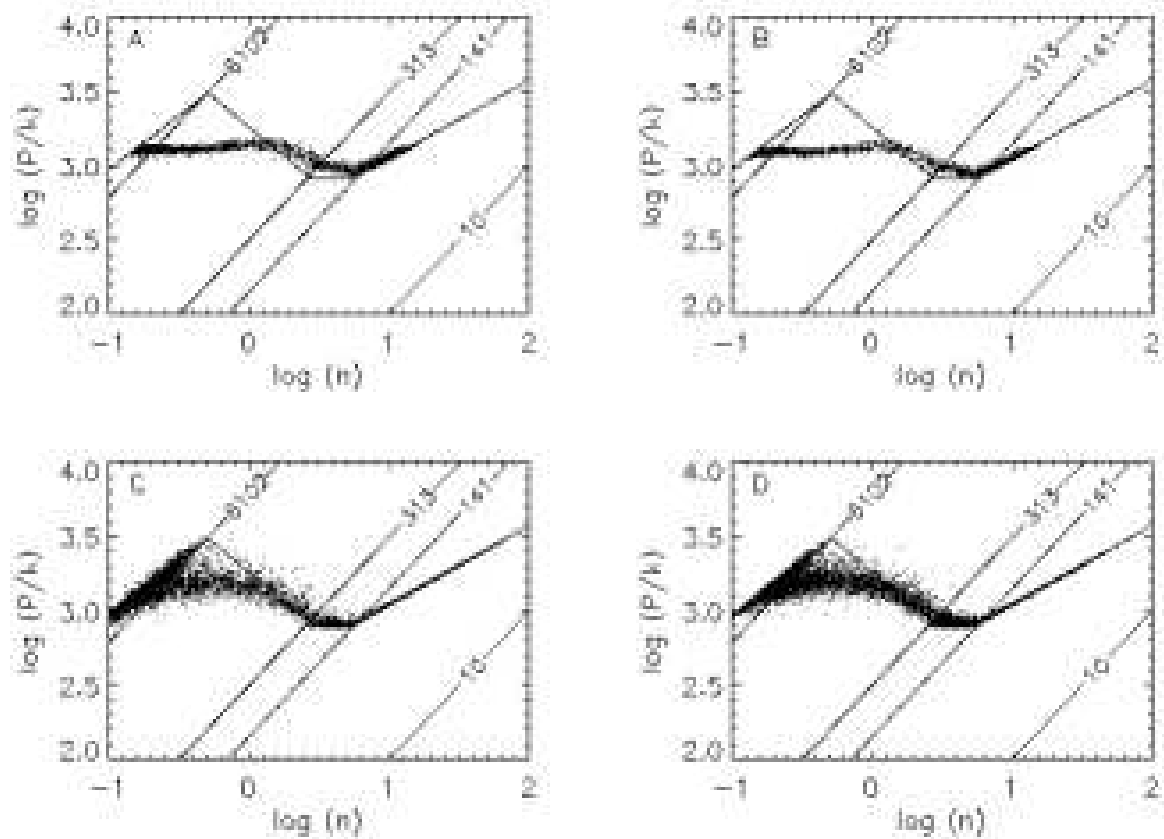


Fig. 7.— Scatter plot of n and P/k for the standard run, at $t = 1, 2.5, 5.0$, and 9 orbits (panels A-D, respectively). The equilibrium cooling curve is plotted for comparison, along with temperature contours corresponding to the transitions between the warm, unstable, and cold phases of gas.

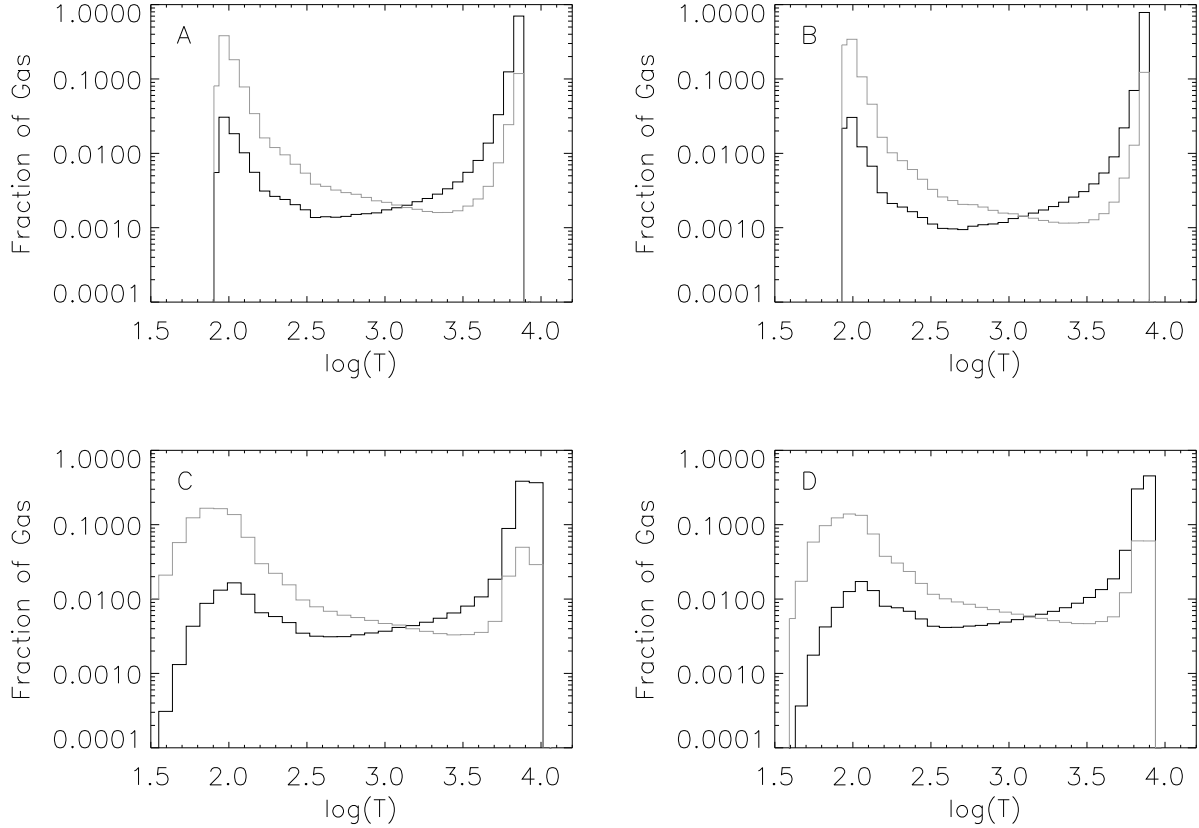


Fig. 8.— Volume (black line) and mass (grey line) temperature PDFs for the standard run at $t = 1, 2.5, 5.0$, and 9 orbits (panels A-D). As for the density PDF, the temperature PDF changes little between Panels A and B. In Panels C and D the development of the MRI forces gas to higher density, which results in the lower temperatures seen in Panels C and D. In addition, the ranges of temperatures for the warm and cold gas peaks also increase.

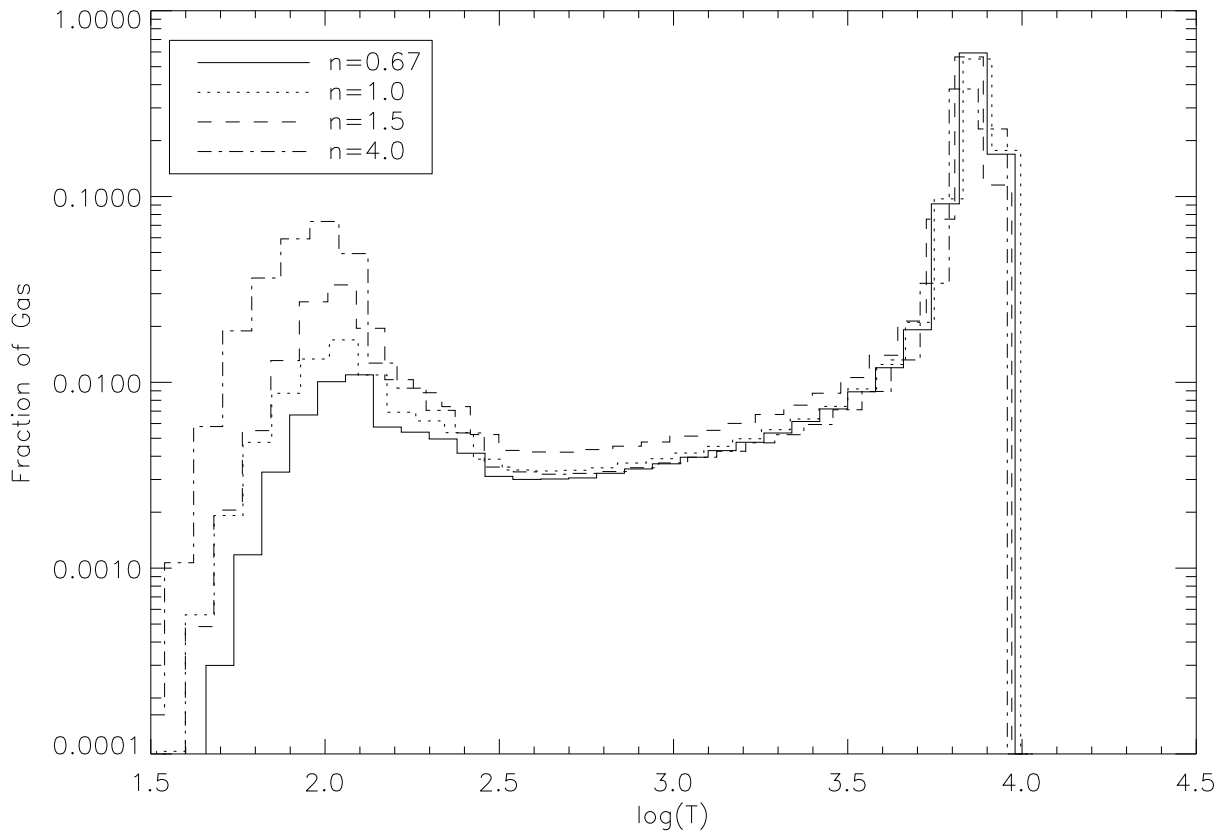


Fig. 9.— Comparison of volume-weighted temperature PDFs for runs with $n = 0.67, 1.0, 1.5$, and 4.0 cm^{-3} , as indicated. The PDFs are averaged over $t = 6.0\text{--}6.5$ orbits. The temperature structure is essentially the same, but as the average density is decreased, the cold gas occupies a smaller total volume, lowering the PDF at low temperature.

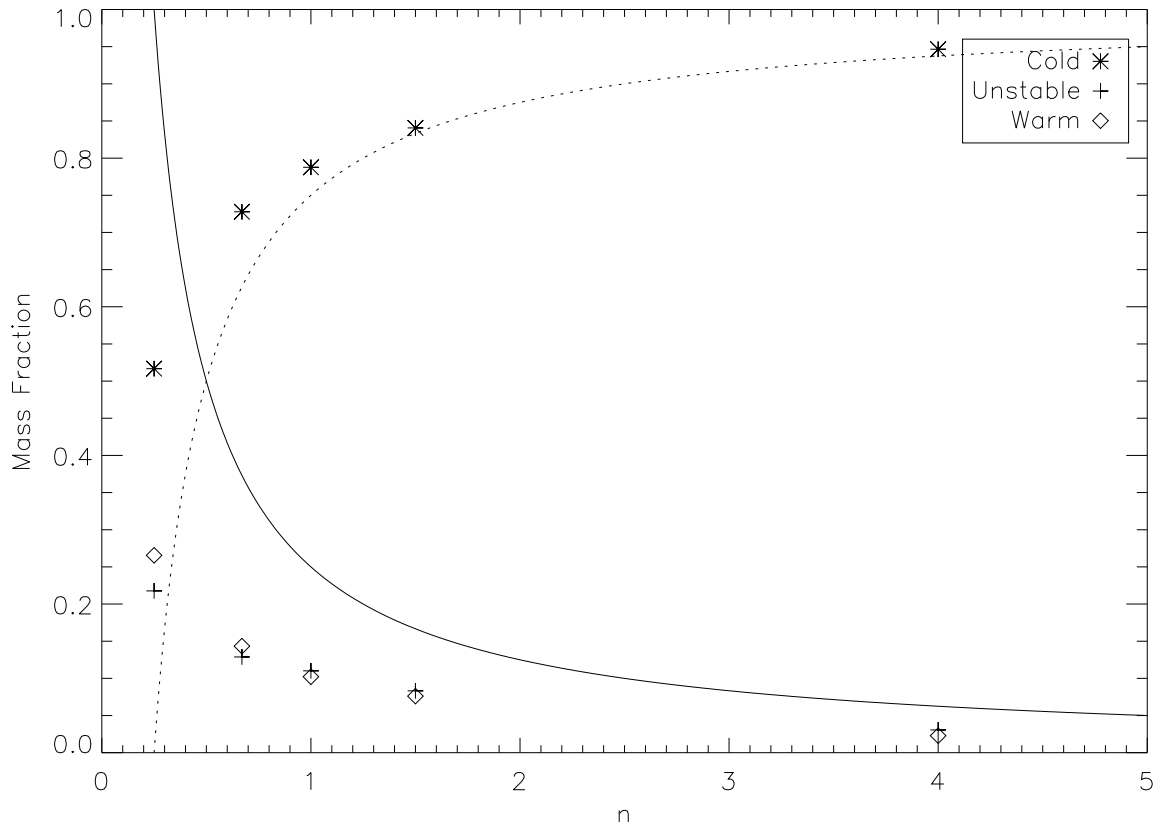


Fig. 10.— Mass fractions for the cold, unstable, and warm phases as a function of mean simulation density, \bar{n} . The dotted and solid lines represent the theoretical mass fractions of the cold and warm phases, respectively, for a perfect two-phase medium in pressure equilibrium, assuming the density of the warm medium is $n_w = 0.25 \text{ cm}^{-3}$, which is typical for our simulations.

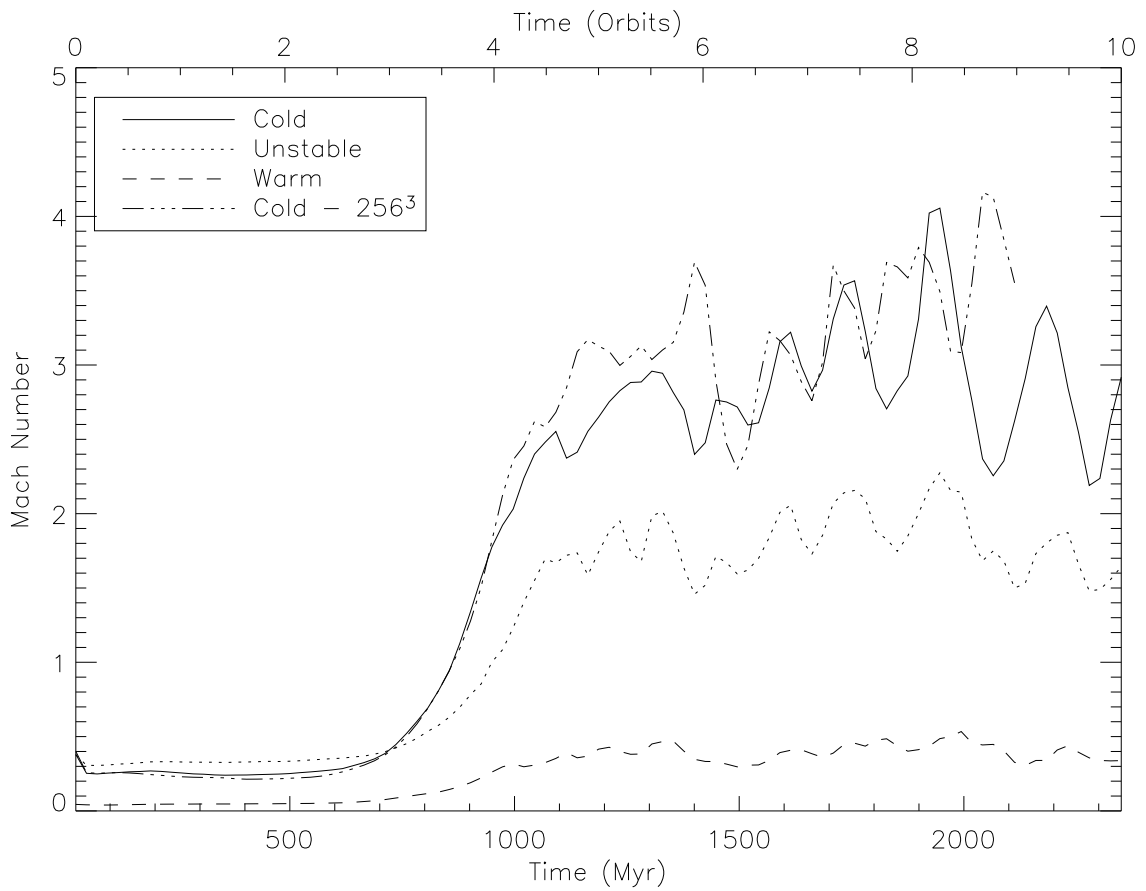


Fig. 11.— Mass weighted Mach number for the three phases of gas in the standard model. The average Mach number for the second half of the simulation is 0.4, 1.8, and 2.9 for the warm, unstable, and cold phases. For comparison we also plot the mass weighted Mach number of the cold medium for the high resolution 256^3 run.

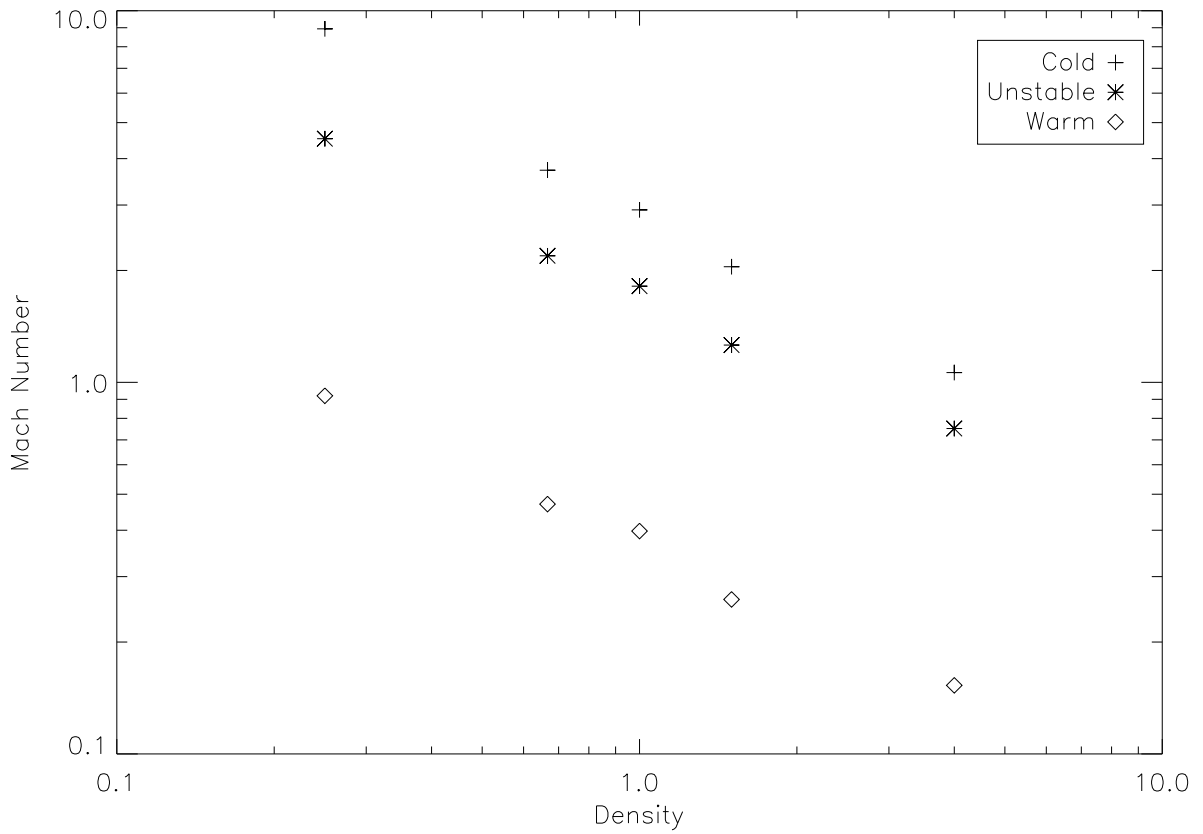


Fig. 12.— Mach number, separated by phase, plotted against the average density in the box for five different simulations. Mean densities of models are $\bar{n} = 0.25, 0.67, 1.0, 1.5$ and 4.0 cm^{-3} . Linear fits to the results give power law slopes of -0.67 , -0.68 and -0.77 for the warm, unstable, and cold phases, respectively.

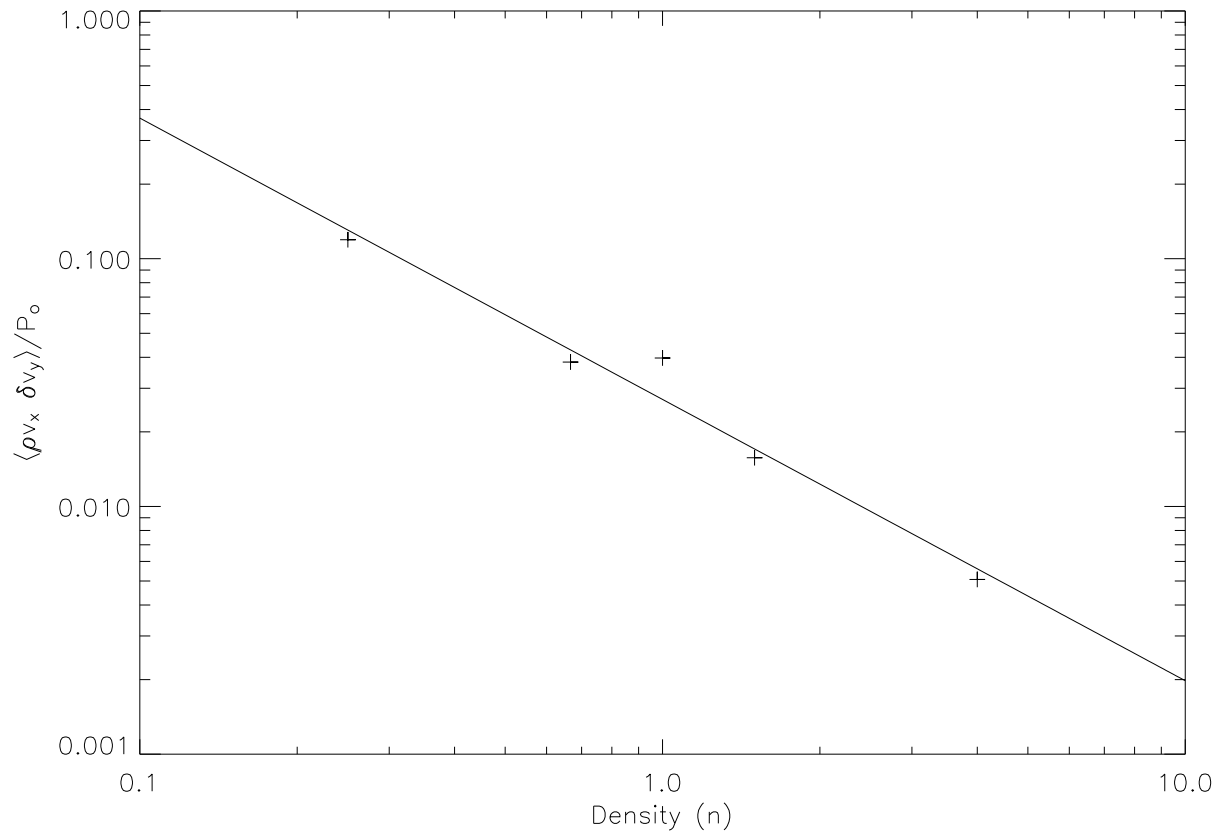


Fig. 13.— Reynolds stress plotted against the mean density for five different simulations with $\bar{n} = 0.25, 0.67, 1.0, 1.5$ and 4.0 cm^{-3} . A fit gives a power law slope of -1.1.

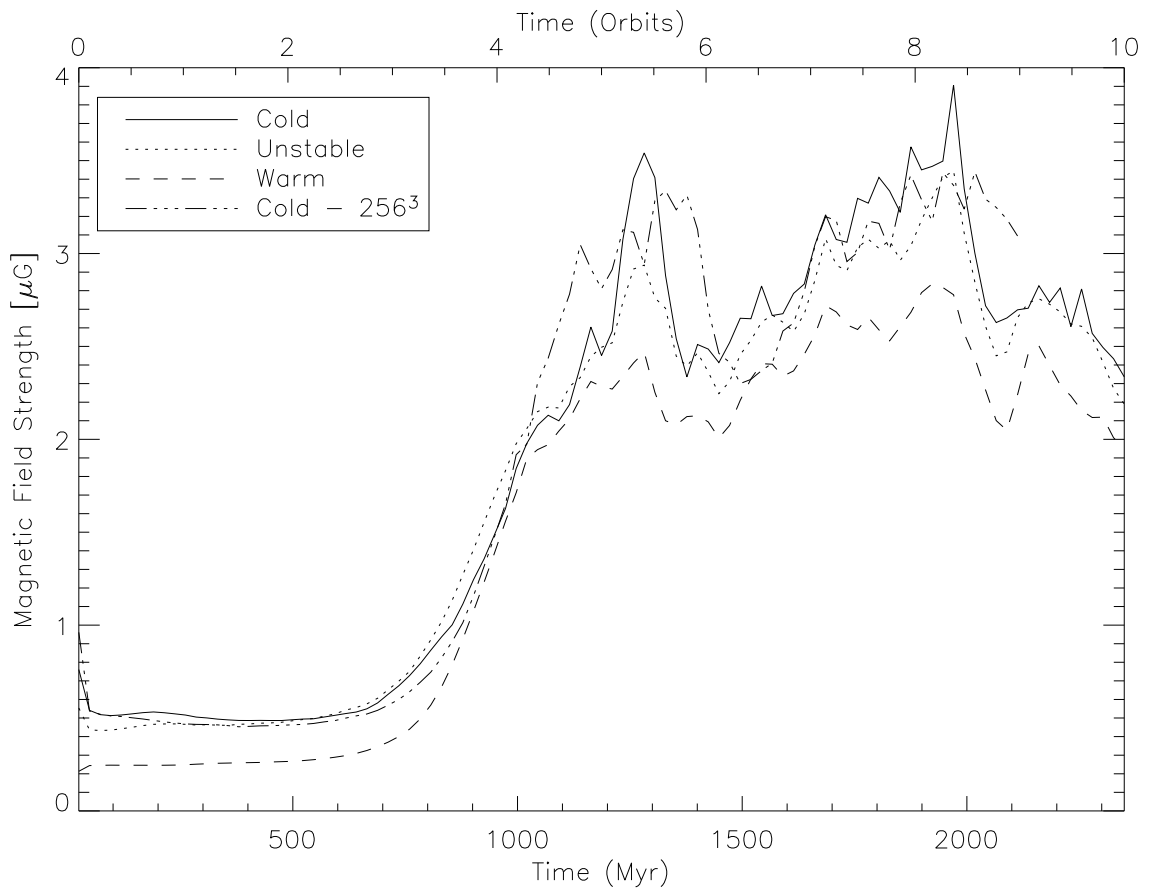


Fig. 14.— Magnetic field strength plotted against time for standard run (with initial $\beta = 100$, i.e. $(B_z)_{\text{init}} = 0.26 \mu\text{G}$). The typical saturated state field strength is $2 - 3 \mu\text{G}$, with little difference between the three phases. For comparison we also plot the field strength in the cold medium for the high resolution 256^3 run.

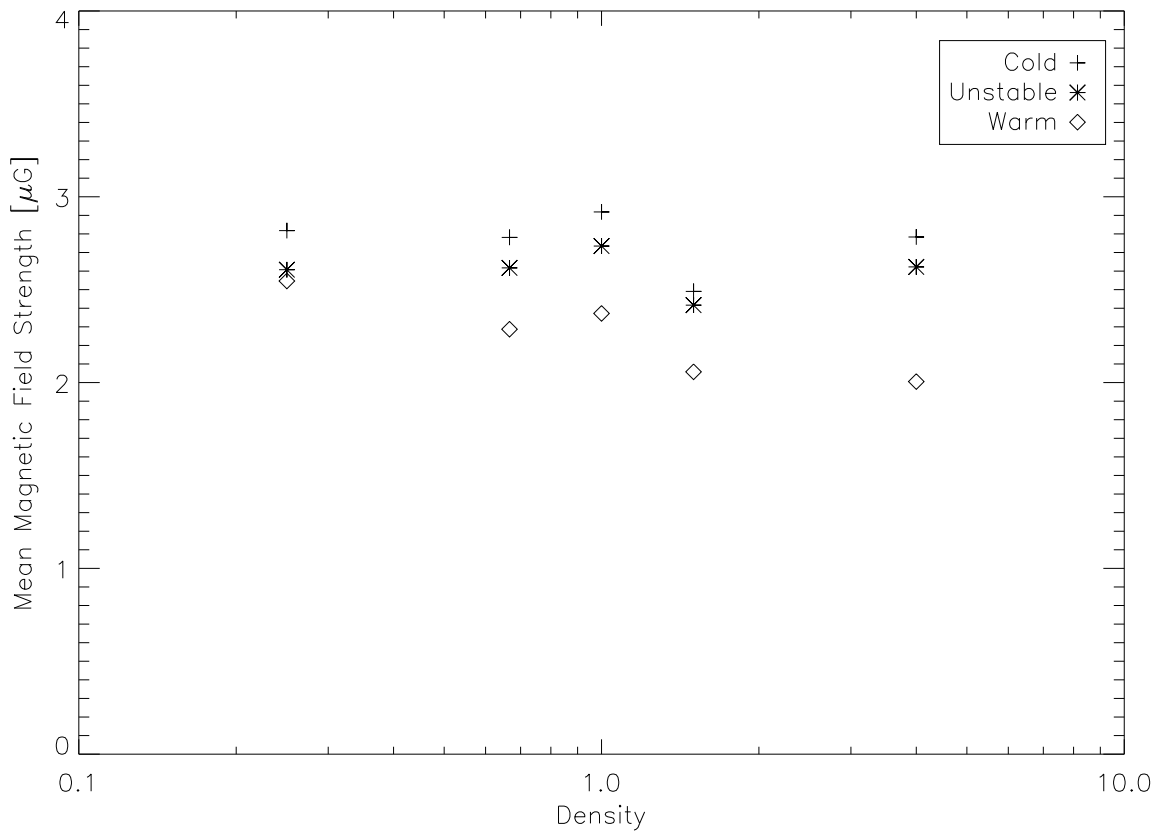


Fig. 15.— Late time magnetic field strength as a function of density for five runs with $\bar{n} = 0.25, 0.67, 1.0, 1.5$ and 4.0 cm^{-3} .

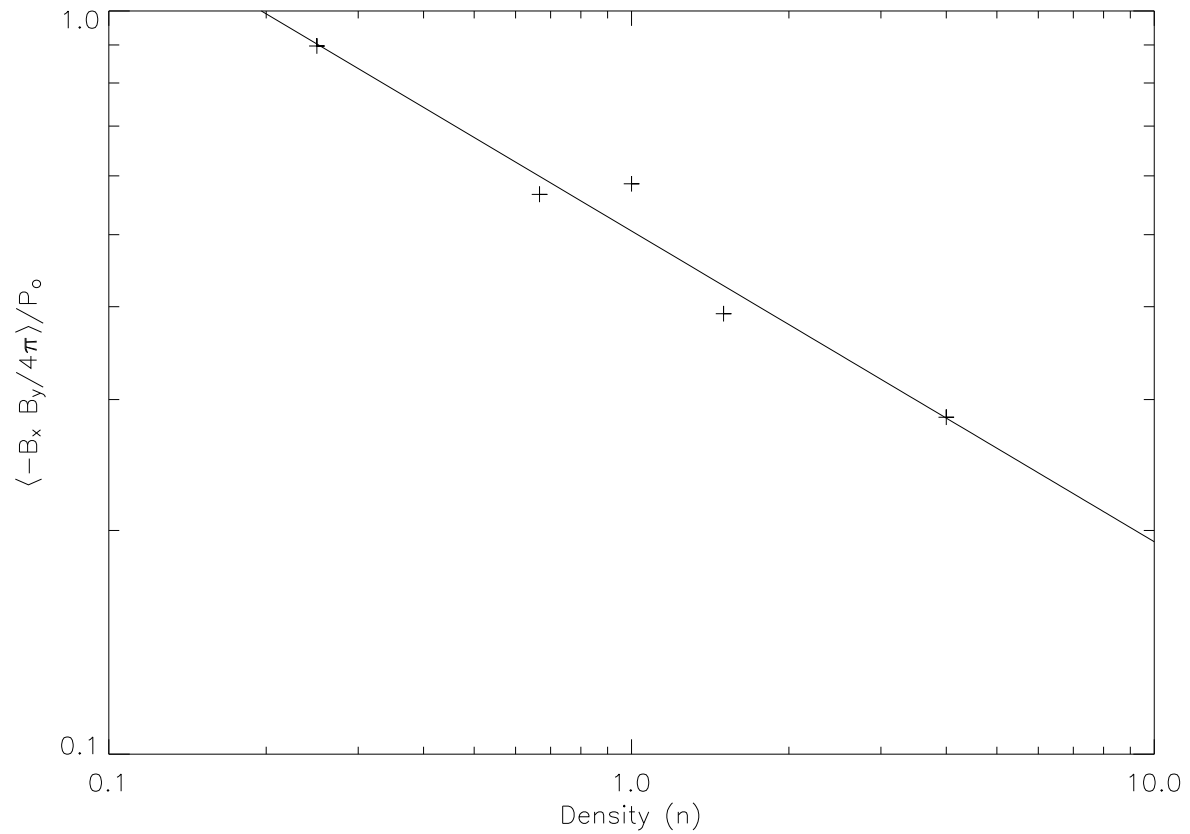


Fig. 16.— Maxwell stress as a function of mean density for five runs with $\bar{n} = 0.25, 0.67, 1.0, 1.5$ and 4.0 cm^{-3} . A fit gives a power-law slope of -0.42.

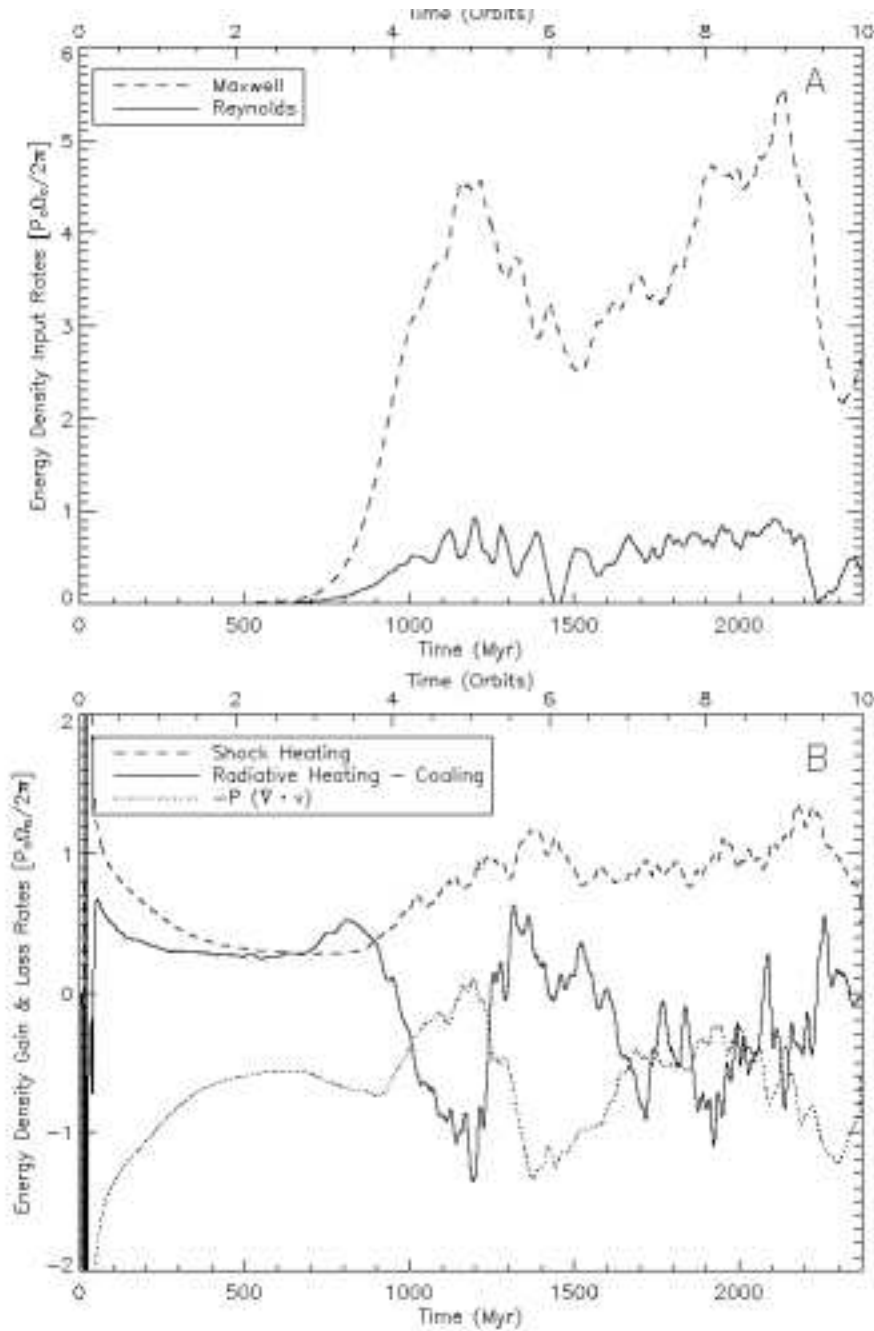


Fig. 17.— In Panel A (upper) we show volume averaged energy input rates from Maxwell and Reynolds stresses plotted against time for a run with standard parameters. In Panel B (lower) we plot the volume averaged energy density gain and loss rates of shock heating, radiative heating - cooling, and $-P(\nabla \cdot v)$ work, plotted against time, for the same run.

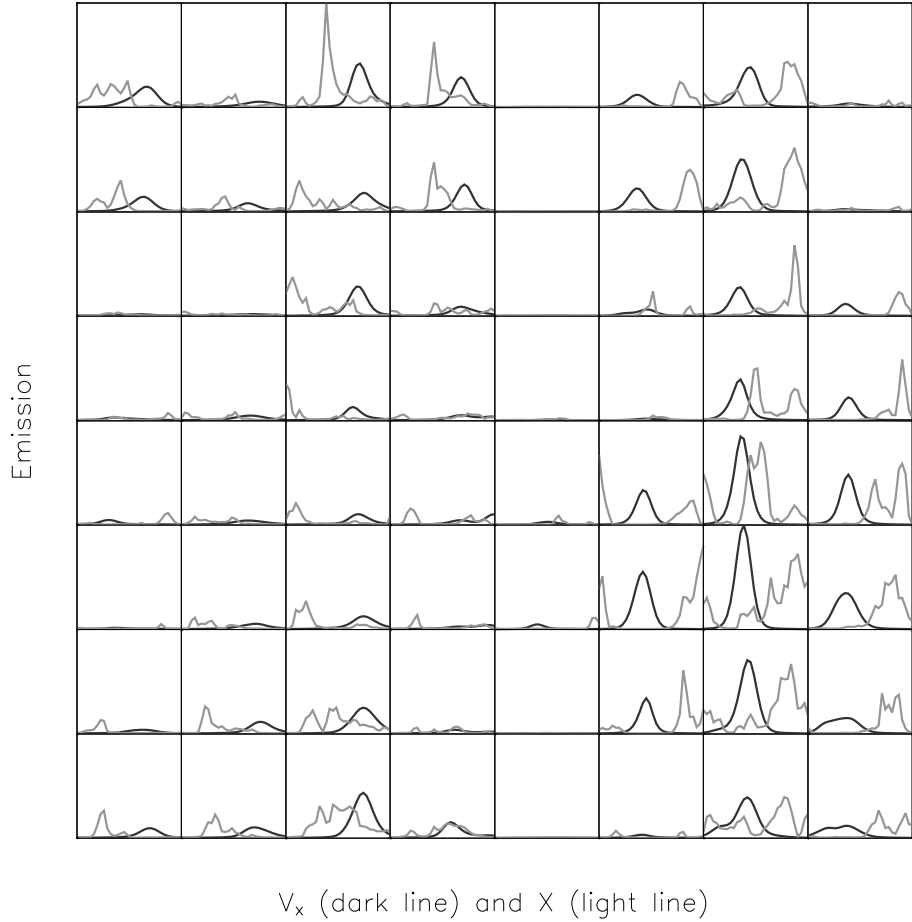


Fig. 18.— Position and velocity profile map in Y-Z plane, for standard run projected along \hat{x} . Dark lines show integrated emission profiles as a function of v_x along the line-of-sight direction. Light lines show profiles of emission as a function of x integrated over line-of-sight velocity.

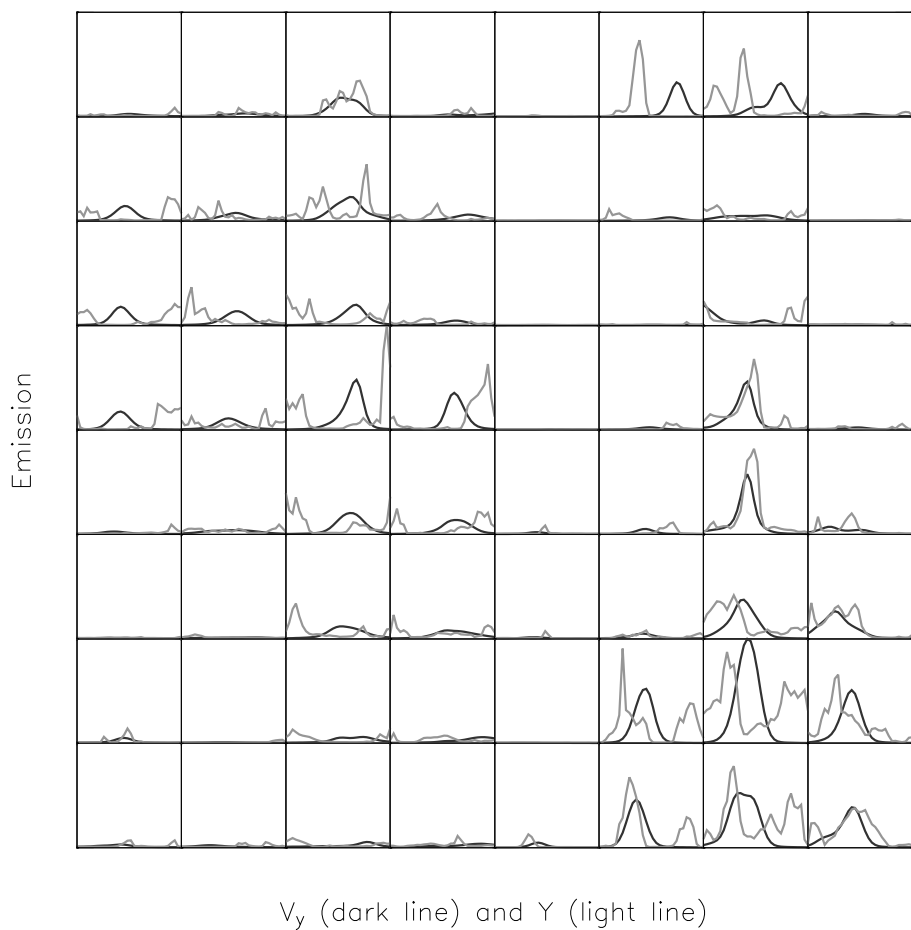


Fig. 19.— Same as Figure 18, for X-Z map projected along \hat{y} .

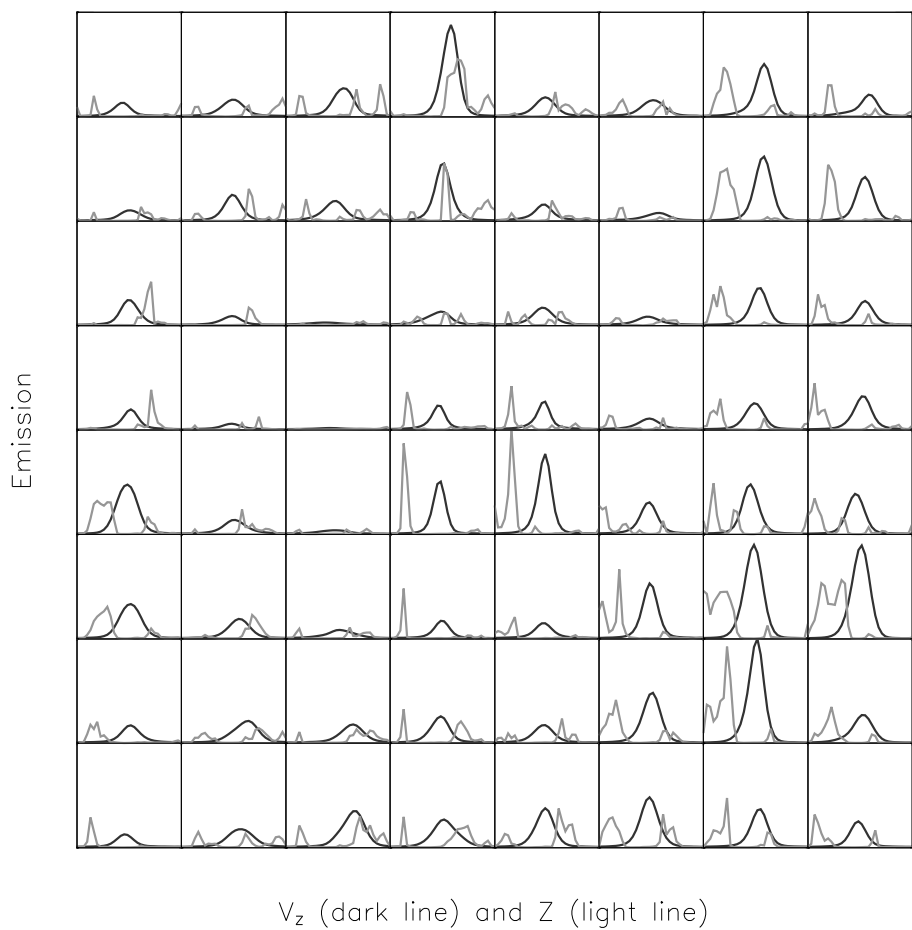


Fig. 20.— Same as Figure 18, for X-Y map projected along \hat{z} .



Fig. 21.— Same as Figure 18, for warm gas only, without thermal broadening.

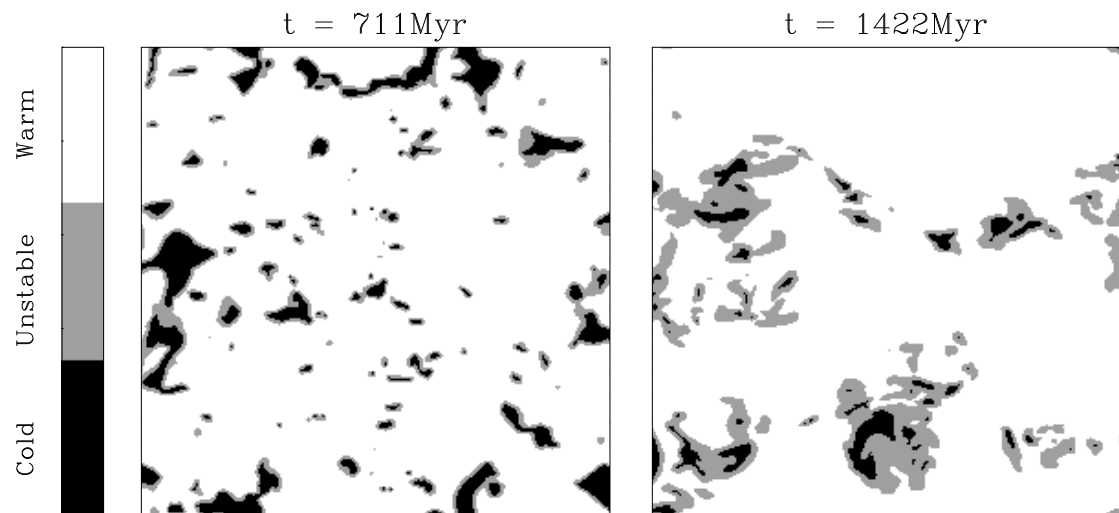


Fig. 22.— A slice at $y=\text{constant}$ through the data cube showing the distribution of cold, unstable, and warm gas, before and after the MRI has begun to dominate the dynamics.